# $K^-p$ Amplitudes near the $\Lambda(1520)$

D. BERLEY AND S. P. YAMIN*
*Brookhaven National Laboratory,† Upton, New York 11973*

AND

R. R. KOFLER, A. MANN, G. W. MEISNER, AND S. S. YAMAMOTO
*University of Massachusetts,‡ Amherst, Massachusetts 01002*

AND

J. THOMPSON§ AND W. WILLIS
*Yale University,‖ New Haven, Connecticut 06520*

(Received 3 November 1969)

$\bar{K}^0n$, $\Lambda\pi^0$, and $\Sigma^0\pi^0$ final-state cross sections and $\Lambda\pi^0$ and $\Sigma^0\pi^0$ polarizations are obtained in $K^-p$ interactions, for $P_{K^-}$ in the range 350–430 MeV/$c$, near the $\Lambda(1520)$ resonance. Two fits to the partial-wave amplitudes have been found, both assuming a standard Breit-Wigner amplitude for the $\Lambda(1520)$ resonance and a constant-scattering-length $D_{3/2}$ isospin-1 amplitude, but differing in their treatment of the $S$- and $P$-wave backgrounds. One method used a constant $K$ matrix, the other a momentum-dependent effective-range expansion for the inverse of the $K$ matrix. From the fitted partial waves, an upper limit of 10% is set for an isospin mixing between the $\Lambda\pi^0$ and $\Sigma^0\pi^0$ amplitudes.

## I. INTRODUCTION

IN this paper we present a study of the following $K^-p$ interactions: $K^-p \to \bar{K}^0n$, $\Sigma^0\pi^0$, and $\Lambda\pi^0$, for incident $K^-$ momenta $P_{K^-}$ in the range 350–430 MeV/$c$. This region is of interest as a link between the threshold and higher-momentum behavior of the $K^-p$ amplitudes and because the presence of the relatively isolated and well-established $\Lambda(1520)$ allows careful study of interference with the other, slowly varying, partial waves. We have previously reported some of the Legendre coefficients for the angular distributions and polarizations and a test of charge independence from the $K^-+p \to \Sigma^0\pi^0$ and $\Lambda\pi^0$ interaction partial-wave amplitudes.[1]

Our momentum range corresponds to center-of-mass energies of 1503–1534 MeV. The $\Lambda(1520)$ with isospin 0 and $J^P=\frac{3}{2}^-$ dominates this region. The lower-energy region is dominated by $S$-wave background waves and the $\Sigma(1385)$ $P_{3/2}$ and $\Lambda(1405)$ $S_{1/2}$ resonances[2–4]; the higher-energy region near the $\Sigma(1660)$ shows a multi-resonance structure which complicates the study of background amplitudes.[5,6] Near the relatively isolated $\Lambda(1520)$, however, $P$- and $D$-wave backgrounds begin to be important, and their interference with the $D_{3/2}$ resonant wave affects the momentum-dependent structure seen in the Legendre coefficients.

The spin and parity of the $\Lambda(1520)$ were determined from a study of $K^-p$, $\Sigma^-\pi^+$, and $\Sigma^+\pi^-$ final states.[7] By combining information from the neutral channels studied in this experiment with the previously published data,[7,8] we have obtained fits for the reaction amplitudes in this region, through $D_{3/2}$, including a small isospin-1 $D_{3/2}$ background wave. Inclusion of this $D_{3/2}$ background has observable effects for $K^-$ momenta greater than about 410 MeV/$c$, but changes the predicted structure only slightly. One fit has been obtained with a constant $K$-matrix[9] parametrization for the background $S$ and $P$ waves; a second fit uses an effective-range expansion of the inverse of the $K$ matrix[10] for these waves. Since the published data on the channels we have not studied are of low statistical accuracy, we cannot expect to make a definitive partial-wave analysis, but only to give a satisfactory framework for the isospin mixing analysis described below.

We have used these fitted amplitudes to place an upper limit on isospin mixing in the observed $\Lambda\pi^0$ and $\Sigma^0\pi^0$ amplitudes. Such mixing would reflect a breakdown

---

* Present address: Physics Department, Rutgers University, New Brunswick, N. J.

† Work performed under the auspices of the U. S. Atomic Energy Commission.

‡ Work supported in part by the U. S. Atomic Energy Commission, under Contract No. AT(30-1)-3651, and in part by a faculty research grant of the University of Massachusetts.

§ Present address: Physics Department, Brookhaven National Laboratory, Upton, N. Y.

‖ Work supported in part by the U. S. Atomic Energy Commission.

[1] J. Thompson, W. Willis, D. Berley, P. Yamin, R. Kofler, A. Mann, G. Meisner, and S. Yamamoto, Bull. Am. Phys. Soc. **14**, 574 (1969); and coefficients reported to R. Levi-Setti, in Rapporteur Talk Proceedings of the Lund International Conference on Elementary Particles, Lund, Sweden, 1969 (unpublished).

[2] W. E. Humphrey and R. R. Ross, Phys. Rev. **127**, 1305 (1962).

[3] M. Sakitt, T. B. Day, R. G. Glasser, N. Seeman, J. Friedman, W. E. Humphrey, and R. R. Ross, Phys. Rev. **139**, B719 (1965).

[4] J. K. Kim, Phys. Rev. Letters **14**, 29 (1965).

[5] L. Bertanza, A. Bigi, R. Carrara, R. Casali, R. Pazzi, D. Berley, E. L. Hart, D. C. Rahm, W. J. Willis, S. S. Yamamoto, and N. S. Wong, Phys. Rev. **177**, 2036 (1969).

[6] J. Meyer, in *Proceedings of the Heidelberg International Conference on Elementary Particles*, edited by H. Filthuth (Interscience, New York, 1968), p. 117.

[7] M. B. Watson, M. Ferro-Luzzi, and R. D. Tripp, Phys. Rev. **131**, 2248 (1963).

[8] R. O. Bangerter, A. Barbaro-Galtieri, J. P. Berge, J. J. Murray, F. T. Solmitz, M. L. Stevenson, and R. D. Tripp, Phys. Rev. Letters **17**, 495 (1966).

[9] R. Dalitz and S. Tuan, Ann. Phys. (N. Y.) **10**, 307 (1960).

[10] G. L. Shaw and M. Ross, Phys. Rev. **126**, 814 (1962).

of charge independence between the isospin pure $\Lambda$ and $\Sigma^0$ particles, or the $\eta$ and $\pi^0$ particles.[11] The method of this isospin mixing test is based on the facts that (1) the $\Lambda(1520)$ has a large branching ratio into the $\Sigma^0\pi^0$ final state, and (2) there are no other nearby resonances which decay into $\Lambda\pi^0$. The measurement then consists in searching for a small resonant $\Lambda\pi^0$ amplitude with $J^P=\frac{3}{2}^-$, characterized by the mass and width of the $\Lambda(1520)$. This amplitude interferes with the nonresonant amplitudes to give a resonant structure in the momentum dependence of the $\Lambda\pi^0$ differential cross section and polarization. Our method is equally sensitive to any phase for such an admixture of the resonant $\Sigma^0\pi^0$ $D_{3/2}$ wave into the other, relatively constant, $\Lambda\pi^0$ waves.

## II. DATA

The data for this experiment come from approximately 340 000 pictures exposed to the AGS low-energy mass-separated $K^-$ beam[12] in the Columbia-Brookhaven 30-in. hydrogen bubble chamber. The run was made in two parts, with central momenta of 375 and 415 MeV/$c$, respectively. The pictures used for this analysis are divided roughly equally between the two runs. In order to extract the momentum dependence of the amplitudes, each run was further divided into $K^-$ momentum bins. All the film was double-scanned for disappearing $K^-$ and neutral $V^0$'s before measurement on conventional, mostly image plane digitizing, machines.

A valid $V$ had its origin a minimum distance (about 4.5 cm in space) from the edge of the picture in view 2, and in addition satisfied the following criteria:

(1) An opening angle greater than 4° in at least one view *and* at most one of the two tracks spirals (electron-pair discrimination).

(2) No clear $\delta$ rays which show that the $V$ is really a $\pi$-$\mu$-$e$ or a $\mu$-$e$ decay (the $\delta$ rays indicate the track direction, and for a true event both tracks leave the decay vertex). The event may also be considered to be a $\pi$-$\mu$-$e$ and rejected if the $\mu$ is less than 1 cm, and there is no origin within 10 cm.

(3) A $V$ is rejected (as a proton-proton scatter) if both arms are short, heavily ionizing, and end in the chamber, and if there is no origin within 10 cm. To be a possible origin for the $V$, a valid 0 prong was required to be at least 5 cm from the edge of the picture, and to have no visible kinks or scatters.

The final states studied are $\bar{K}^0n$, $\Lambda\pi^0$, and $\Sigma^0\pi^0$, with the $\Sigma^0\pi^0$ reaction observed through the decay $\Sigma^0\to\Lambda\gamma$. About 60 000 events were processed through the geometry and kinematics programs.[13] The fits attempted are shown in Table I; they include a one-constraint (1C) and a three-constraint (3C) decay fit for both $\bar{K}^0$ and $\Lambda$ hypotheses, and a 1C production fit if either of the appropriate decay fits was successful.

TABLE I. Kinematic fits performed.

| No. of constraints | Process | Input |
|---|---|---|
| 1 | $\Lambda$ decay $\to p\pi^-$ | $p$, $\pi^-$ measured, $\Lambda$ mass |
| 1 | $\bar{K}^0$ decay $\to\pi^+\pi^-$ | $\pi^+\pi^-$ measured, $\bar{K}^0$ mass |
| 3 | $\Lambda$ decay $\to p\pi^-$ | $p$, $\pi$ measured, $\Lambda$ mass, two-point direction ($K^-$ end to $V$ vertex) |
| 3 | $\bar{K}^0$ decay $\to\pi^+\pi^-$ | $\pi^+\pi^-$ measured, $\bar{K}^0$ mass, two-point direction |
| 1 | $K^-p\to\Lambda\pi^0$, production | $\Lambda$ from 3C (1C) decay fit, $K$ measured, $\pi^0$ mass |
| 1 | $K^-p\to\bar{K}^0n$, production | $K^0$ from 3C (1C) decay fit, $K^-$ measured, $n$ mass |

About 20 000 events fell in one of the following categories and were remeasured:

(1) Events scanned but not measured.

(2) Events with tracks rejected by the geometry program.

(3) No successful kinematic fit.

(4) Events with only a $\bar{K}^0$-decay fit.

(5) Events which fail $\chi^2$ criteria for the 3C $\Lambda$-decay fit but which pass criteria for $\Lambda\pi$ production or the 1C $\Lambda$-decay fit. (Because of the short $\Sigma^0$ lifetime, the $\Lambda$'s from the $\Sigma^0\pi^0$ events, as well as from the $\Lambda\pi^0$ events, will point to the associated $K^-$.)

(6) Events for which the effective mass of the $V$, calculated from geometry output, was neither that of a $\Lambda$ ($1100<\Lambda$ effective mass$<1135$ MeV) nor that of a $\bar{K}^0$ ($473<K^0$ effective mass$<523$ MeV).

(7) Events which fail 3C $\bar{K}^0$-decay fit criteria but pass 1C decay or $\bar{K}^0n$ production criteria; however, if these events had 3C $\Lambda$-decay fits and were inside the $\Lambda$ effective mass cuts, they were not remeasured.

(8) Events with negative missing mass squared from $K^-+p\to\Lambda+$missing mass.

Events were remeasured only if the $V^0$ length was greater than 1 mm, since, as is described below, a cut of 2 mm was made on $V^0$ length.

The $\bar{K}^0$ and $\Lambda$ decays can be separated by kinematics without much difficulty, especially since all the $\bar{K}^0$'s come from the two-body charge-exchange reaction. An event is classified as a $\bar{K}^0$ if it makes a $\bar{K}^0n$-production or -decay fit and no $\Lambda$-decay fit. An event is classified as a $\Lambda$ if it makes a 3C $\Lambda$-decay fit and, in addition, either (1) it makes no $\bar{K}^0n$-production fit or (2) the positive track is identified as a proton from range. For events which are ambiguous between a $\bar{K}^0$ and a $\Lambda$ interpretation and for events with poorly measured tracks, corrections were made to the cross-section estimates from results of scan-table examination of a

[11] C. H. Chan and A. Q. Sarker, Nuovo Cimento **36**, 1402 (1965).
[12] D. Berley, Alternating Gradient Synchrotron Division Technical Report No. 258, 1965 (unpublished).
[13] The geometry program used is NP-54, developed at Columbia University; the kinematic program used is HASH, developed at the University of Wisconsin.

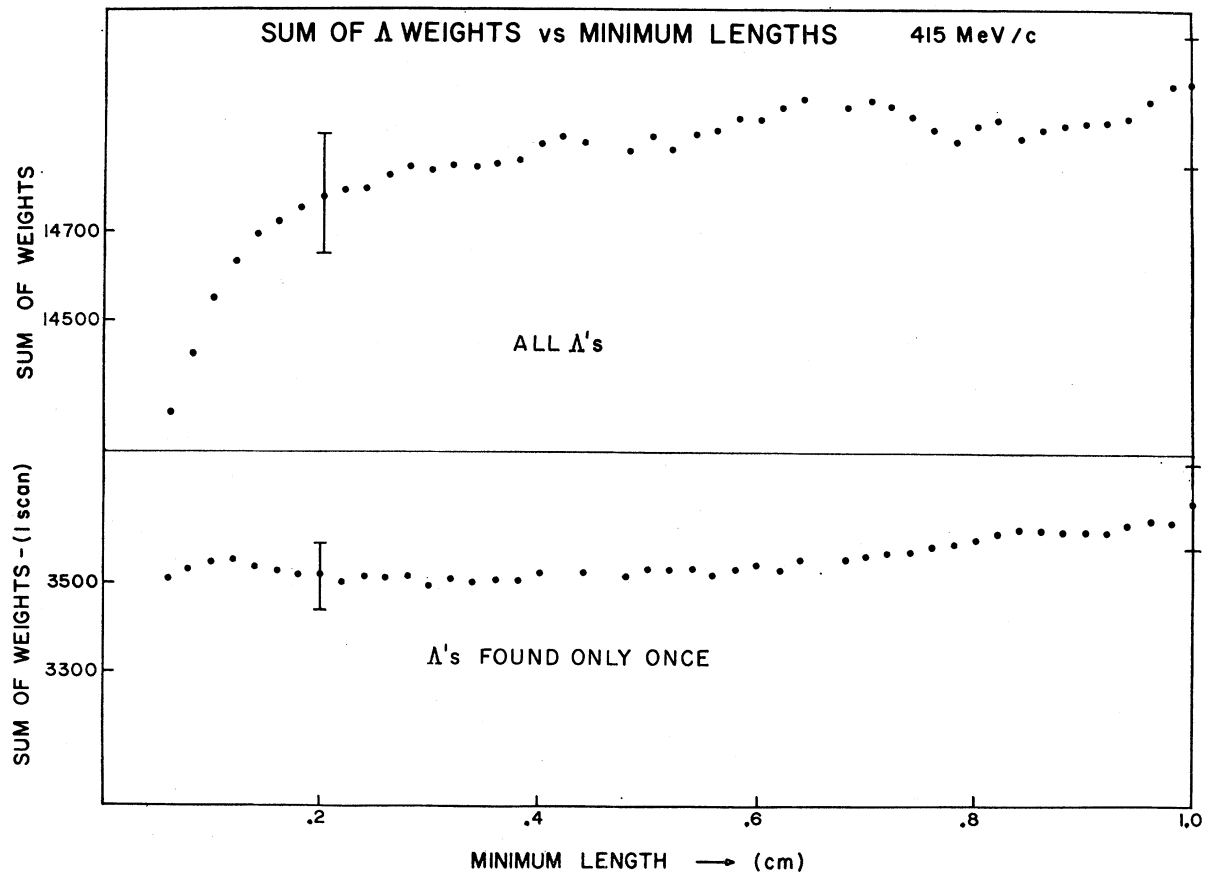


FIG. 1. Sums of Λ weights versus minimum cutoff length for the Λ. This distribution is expected to be constant in the region of satisfactory cutoff length. (top) Sum of weights for all Λ's found. (bottom) Sum of weights for Λ's found only once in the double scan.

sample of events. The $\chi^2$ cuts (20 for 3C decay fits, 6 for 1C decay fits, and 10 for 1C production fits) were also based on these scan-table results.

The $V$'s were required to have a projected length of greater than 2 mm in the scan plane and to be inside a truncated cone which represents the useful volume seen from view 2. A weight $w$, computed for each event, compensates for these cuts:

$$w=\frac{1}{e^{-t_{\min}}-e^{-t_{\text{fid}}}}=\frac{1}{\text{probability of a } V \text{ decay within the cuts}},$$

where $t_{\min}$ is the proper time in units of the $V$ mean life for the $V$ to travel the projected minimum length, and $t_{\text{fid}}$ is the time at which the $V$ leaves the fiducial volume. A further, nonanalytic weight compensates for the scanning and measuring loss of $V$'s with short prongs and extreme opening angles. These losses appear as depletions in a plot of the direction cosine of the positive track with respect to the $V$, in the $V$ center-of-mass system ($\mathbf{u}_+\cdot\mathbf{V}$). For the full sample of true events, this distribution would be isotropic. From the depletions near $\mathbf{u}_+\cdot\mathbf{V}=\pm1$, for different production angle bins, an empirical weight is found as a function of the production angle. Since these short-prong and opening-angle losses are particularly severe for the very-low-momentum $V$'s produced at large angles with respect to the beam direction, we excluded from the analysis events with center-of-mass $V$ production-angle cosines between $-0.9$ and $-1$. The weighted numbers of all events found, and of events found in only one of the two scans, are shown for different cutoff lengths for a sample from the high-momentum film in Figs. 1 and 2.

The flatness of these curves above our chosen cutoff length of 2 mm indicates that above this cutoff the weighted number of events is relatively constant. Comparison of the curves for all events found and for those found only once indicates that the same cutoff length can be used for both. Similar behavior is found for events from the low-momentum film. From Figs. 5 and 6 we can compute the efficiency of a single scan as follows:

$E_1=$ (single-scan efficiency)
$=1-$(events lost by 1 scanner)/(all events)
$\approx1-\frac{1}{2}$(events found only once)/(all events found),

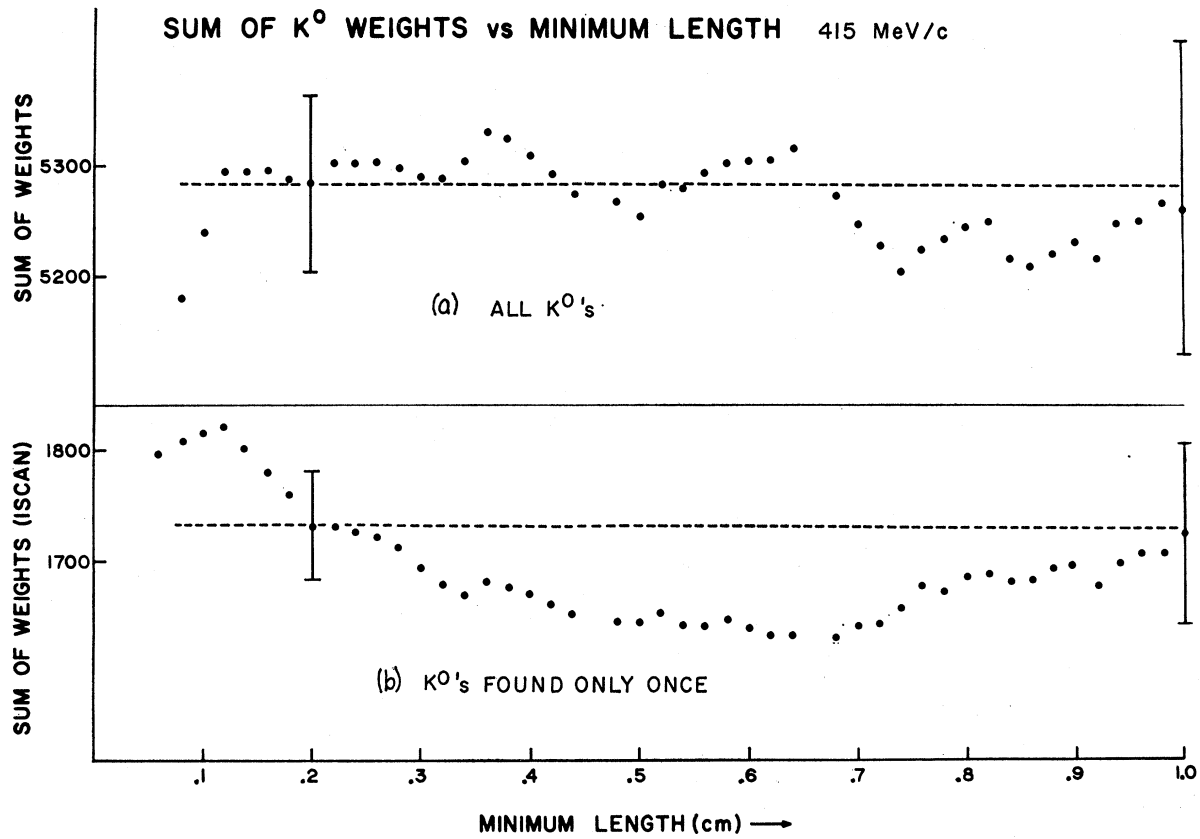


FIG. 2. Sums of $\bar{K}^0$ weights versus the minimum $\bar{K}^0$ cutoff lengtn for the $\bar{K}^0$. The distribution is expected to be constant in the region of satisfactory cutoff length. (a) Sum of weights for all $\bar{K}^0$'s found. (b) Sum of weights for $\bar{K}^0$'s found only once in the double scan.

where all events are approximately the same as all events found. The double-scan efficiency is then

$$E_2 = (\text{double-scan efficiency}) = (\text{events found})/(\text{all events}) = E_1 + (1-E_1)E_1.$$

Figures 1 and 2 show, then, a single- (double-) scan efficiency of 88% (98.9%) for $\Lambda$'s and 84% (97%) for $K$'s for the minimum cutoff length of 0.2 cm.

## III. LEGENDRE COEFFICIENTS

Any production-angle distribution can be conveniently expressed as a Legendre series expansion:

$$\frac{d\sigma}{d\Omega} = 4\pi\lambda^2 \sum_{l=0}^{N} a_l P_l(\cos\theta),$$

where $d\sigma/d\Omega$ is in (fermi)$^2$. For our case, $\theta$ is the center-of-mass angle between the $K^-$ and the final-state meson and $(1/\lambda)$ is the $K^-$ center-of-mass momentum in units of $\hbar$. It has been found sufficient to include terms up to $l=3$ for our experiment. For the kinematically constrained $\bar{K}^0n$ reaction, the usual method-of-moments calculation has only to be modified to take into account the production-angle cuts. A histogram of the observed $\bar{K}^0n$ angular distribution for the momentum bin from the higher-momentum film with $P_{K^-}$ between 380 and 400 MeV/$c$ is compared with the fitted distribution in Fig. 3.

For the $\Lambda\pi^0$ and $\Sigma^0\pi^0$ reactions, there is partial kinematic overlap since only the $\Lambda$ in the final states is observed. This can be seen most clearly in Fig. 5, which shows the missing mass squared, defined by $K^-+p \rightarrow \Lambda+$missing mass. Before allowing for experimental resolution, the $\Lambda\pi^0$ reaction gives events at $(m_{\pi^0})^2$ and the $\Sigma^0\pi^0$ reaction gives events in a uniform distribution with missing mass squared from $\approx 1.2$ $(m_{\pi^0})^2$ to $\approx 6.7(m_{\pi^0})^2$. The existence of the $\Lambda\pi^0\pi^0$ and $\Sigma^0\pi^0\pi^0$ reactions makes it undesirable to use events with missing mass squared greater than $4(m_{\pi^0})^2$. An investigation of the experimental resolution function shows that it approximates a Gaussian for a fixed $K^-$ momentum and $\cos\theta$, but that the width of the Gaussian varies widely as a function of $\cos\theta$. Thus, using a fixed missing-mass cut would include different fractions of the $\Lambda\pi^0$ and $\Sigma^0\pi^0$ channels at different angles. Therefore, we have made a fit to a full distribution function for the observed $\Lambda$ decays from both $\Lambda\pi^0$ and $\Sigma^0\pi^0$ production channels. The distribution function $F(x,\mathfrak{M})$ depends on

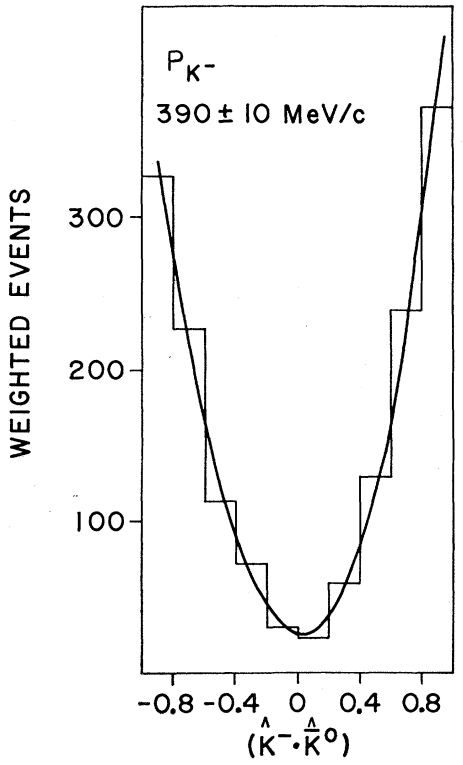


FIG. 3. $\bar{K}+p \to \bar{K}^0 n$ weighted angular distribution for the higher-momentum film, with $P_{K^-}$ from 380 to 400 MeV/$c$. The smooth curve is generated from the coefficients determined from only the events with the c.m. $K^-$-$\bar{K}^0$ direction cosine$>-0.9$.

$\cos\theta$ $(x)$ and missing mass squared $(\mathfrak{M})$:

$$F(x,\mathfrak{M})=\sum_l [A_l{}^\Lambda P_l(x) f_\Lambda(x,\mathfrak{M})+a_l{}^\Sigma P_l(x) f_\Sigma(x,\mathfrak{M})], \quad (1)$$

where $A_l{}^\Lambda$ are the Legendre series coefficients for the $\Lambda\pi^0$ angular distribution and the $a_l{}^\Sigma$ are the coefficients for the observed $\Lambda$ from the $\Sigma^0\pi^0$ channel. The functions $f_\Lambda$ [a Gaussian centered at $(m_{\pi^0})^2$] and $f_\Sigma$ (a sum of Gaussians corresponding to the possible ideal $\mathfrak{M}$ values) describe the missing-mass-squared distributions; they are also functions of $\cos\theta$ because of the experimental resolution dependence on the angle. We approximate the angle-dependent width of the Gaussians by $\sigma(x)$, a third-order polynomial in $x$; we can then write $f_\Lambda$ and $f_\Sigma$:

$$f_\Lambda(x,\mathfrak{M})=\frac{1}{(2\pi)^{1/2}\sigma(x)}\exp\left[-\left(\frac{\mathfrak{M}-m_{\pi^0}{}^2}{\sqrt{2}\sigma(x)}\right)^2\right]$$

and

$$f_\Sigma(x,\mathfrak{M})=P_\Sigma(x,\mathfrak{M})\Big/\int d\mathfrak{M}' P_\Sigma(x,\mathfrak{M}'),$$

where

$$P_\Sigma(x,\mathfrak{M})=\int\frac{dm^2}{(2\pi)^{1/2}\sigma(x)}\exp\left[-\left(\frac{\mathfrak{M}-m^2}{\sqrt{2}\sigma(x)}\right)^2\right].$$

The method of moments is used to solve Eq. (1). The expectation values for the factors

$$P_l(\cos\theta) f_\Lambda(\cos\theta,\mathfrak{M})$$

and

$$P_l(\cos\theta) f_\Sigma(\cos\theta,\mathfrak{M}),$$

averaged over missing mass and $\cos\theta$, are calculated in two ways. The first method is used to calculate the moment $M_n{}^Y$ (as a function of the $a_l{}^\Sigma$ and $A_l{}^\Lambda$) from the distribution function definition by integrating over

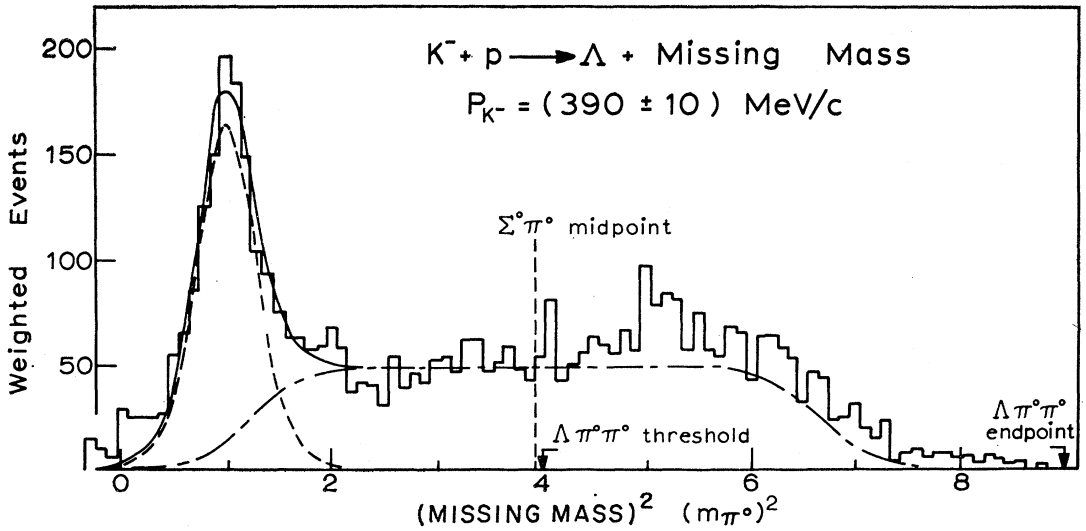


FIG. 4. Observed histograms and fitted curves for the missing mass squared from $K^-+p \to \Lambda+$missing mass, for events in the momentum bin from the higher-momentum film with $P_{K^-}$ from 380 to 400 MeV/$c$. The dashed and dot-dashed curves are fitted curves for $\Lambda\pi^0$ and $\Sigma^0\pi^0$, respectively; the solid curve is the sum of the $\Lambda\pi^0$ and $\Sigma^0\pi^0$ curves. Only events with missing mass squared below the $\Sigma^0\pi^0$ midpoint are used.

$\cos\theta$ from $-1$ to 0.9 and missing mass squared up to the midpoint of the $\Sigma^0\pi^0\mathfrak{M}$ distribution:

$$M_n{}^Y=\int\int d\cos\theta\, d\mathfrak{M}\, f_Y(\cos\theta,\mathfrak{M})P_n(\cos\theta)F(\cos\theta,\mathfrak{M})$$
$$=\sum_l (C_{nl}{}^{\Lambda Y}A_l{}^\Lambda+C_{nl}{}^{\Sigma Y}a_l{}^\Sigma),$$

where

$$C_{nl}{}^{YY'}=\int\int d\cos\theta\, d\mathfrak{M}\, P_l(\cos\theta)P_n(\cos\theta)$$
$$\times f_Y(\cos\theta,\mathfrak{M})f_{Y'}(\cos\theta,\mathfrak{M}).$$

In the expressions above, $Y$ is the hyperon index and has the value 1 for $\Lambda$'s and 2 for $\Sigma^0$'s. The second method calculates the "observed" moment $Q_n{}^Y$ as a weighted average over the experimental events, using the same cuts on $\cos\theta$ and $\mathfrak{M}$ as the integration limits for the $M_n{}^Y$ calculation. This method yields a number depending on the experimental events:

$$Q_n{}^Y=\sum w_i f_Y(\cos\theta_i,\mathfrak{M}_i)P_n(\cos\theta_i).$$

The method of moments allows us (in the limit of large numbers) to set the two expectation values equal, leading to a set of linear equations for the $A_l{}^\Lambda$ and $a_l{}^\Sigma$:

$$Q_n{}^Y=M_n{}^Y$$
$$=\sum(C_{nl}{}^{\Lambda Y}A_l{}^\Lambda+C_{nl}{}^{\Sigma Y}a_l{}^\Sigma).$$

This can be written as a matrix equation $\mathbf{Q}=\mathbf{CA}$ if we form the vectors $\mathbf{Q}=(Q_0{}^\Lambda, Q_1{}^\Lambda,\ldots, Q_N{}^\Lambda, Q_0{}^\Sigma, Q_1{}^\Sigma,\ldots, Q_N{}^\Sigma)$ and $\mathbf{A}=(A_0{}^\Lambda,\ldots, A_N{}^\Lambda, a_0{}^\Sigma,\ldots, a_N{}^\Sigma)$ and the matrix

$$\mathbf{C}=\begin{bmatrix}\mathbf{C}^{\Lambda\Lambda} & \mathbf{C}^{\Lambda\Sigma}\\ \mathbf{C}^{\Lambda\Sigma} & \mathbf{C}^{\Sigma\Sigma}\end{bmatrix},$$

where the $C_{nl}{}^{YY'}$, elements of the submatrices $\mathbf{C}^{YY'}$, have been defined above.

This matrix equation may then be inverted, yielding $A_l{}^\Lambda$ and $a_l{}^\Sigma$, which describe the angular distributions of the observed $\Lambda$'s from the $\Lambda\pi^0$ and $\Sigma^0\pi^0$ reactions. To illustrate the effectiveness of this calculation, the coefficients for the set of events from the higher-momentum film in the momentum bin with $K^-$ momentum $390\pm10$ MeV/$c$ are used to generate the fitted angular distributions and the fitted missing-mass-squared spectrum integrated over $\cos\theta$. These distributions are compared with the experimental histograms in Figs. 4 and 5. Figure 6 shows the missing-mass histograms for samples in different regions of $\cos\theta$; these have quite different appearances but are fitted well by the generated distributions.

From the total number of events with missing mass squared above the $\Sigma^0\pi^0\mathfrak{M}$ midpoint, less the number predicted from the $\Sigma^0\pi^0$ curve, the three-body cross sections shown in Fig. 7 are estimated. From the known ratio $\Sigma^0\pi^+\pi^-/\Lambda\pi^+\pi^-$,[7,14] these neutral three-body events are expected to be about 97% $\Lambda\pi^0\pi^0$ and 3% $\Sigma^0\pi^0\pi^0$.

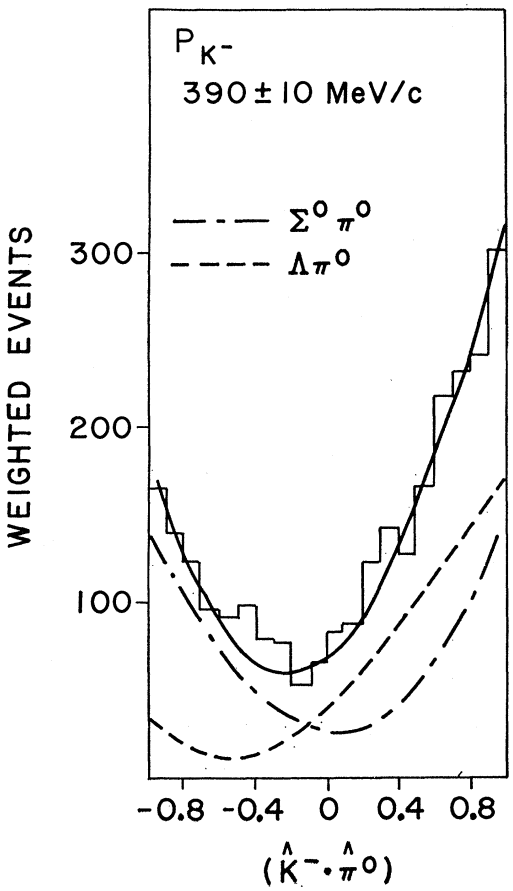


FIG. 5. For the events in Fig. 4 below the $\Sigma^0\pi^0$ missing mass squared spectrum midpoint, the histogrammed weighted angular distribution is shown. The smooth curves are generated from the fitted coefficients: $\Lambda\pi^0$ (dashed curve), $\Sigma^0\pi^0$ (dot-dashed curve), and the $\Lambda\pi^0$ and $\Sigma^0\pi^0$ sum (solid curve) which is to be compared with the observed histogram. The fitted coefficients are determined using only the events with the c.m. $K^-$-$\Lambda$ direction cosine $>-0.9$.

The $a_l{}^\Sigma$ computed by the above method may be related to the true coefficients $A_l{}^\Sigma$ through the kinematics of the isotropic $\Sigma^0\to\Lambda+\gamma$ decay. The $A_l{}^\Sigma$, which we report, are given by a factor depending on $l$, times the $a_l{}^\Sigma$. The calculation of these factors, typically a correction of a few percent at these momenta, is described in the Appendix.

Polarization expansion coefficients are found in a similar manner, using

$$F(x,\mathfrak{M})\mathbf{P}\cdot\hat{n}=(\sin\theta)\sum_l \frac{dP_l(\cos\theta)}{d(\cos\theta)}$$
$$\times[B_l{}^\Lambda f_\Lambda(x,\mathfrak{M})+b_l{}^\Sigma f_\Sigma(x,\mathfrak{M})]$$

[14] S. B. Chan, University of Massachusetts (private communication).

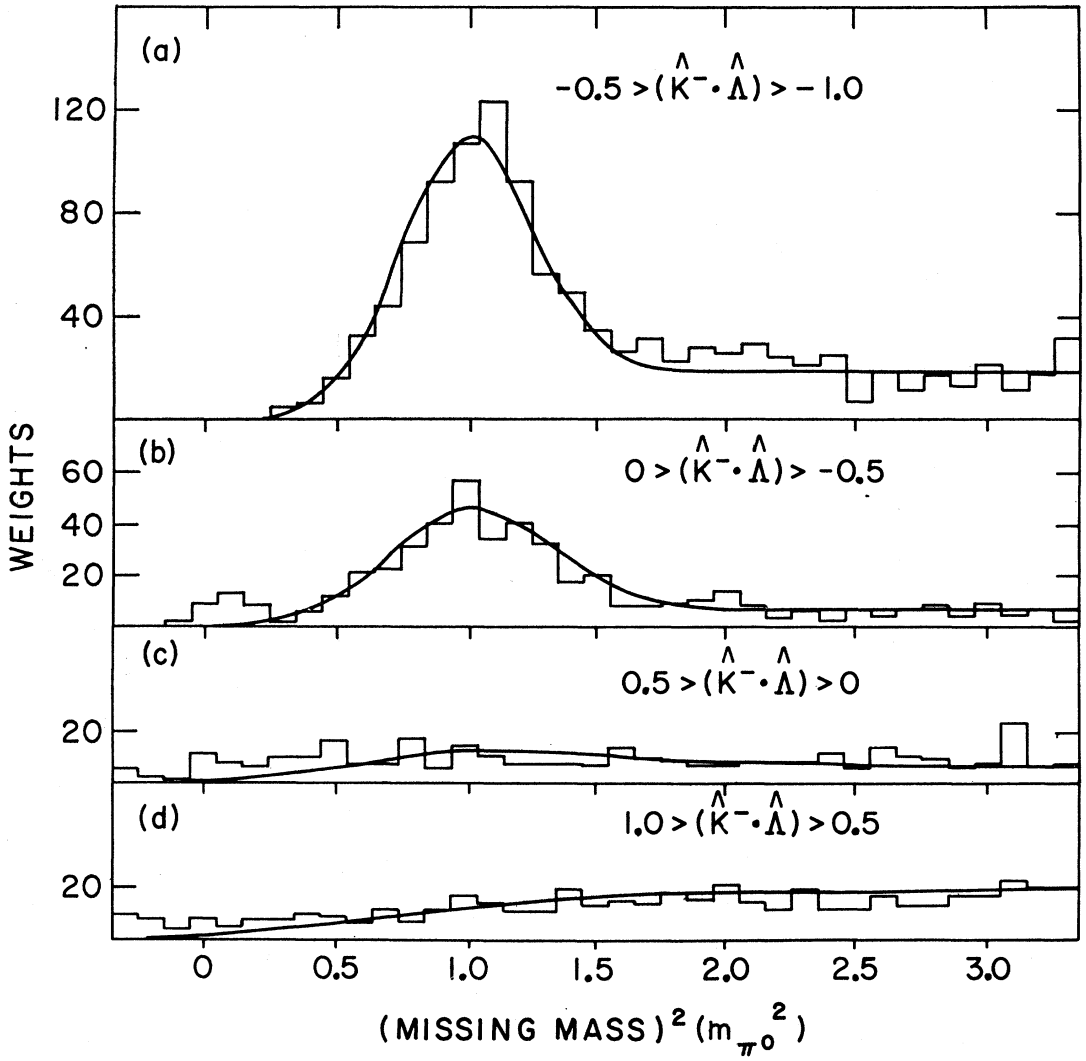


FIG. 6. Weighted missing mass squared spectra for the events from Fig. 4, divided into bins in $(K^- \cdot \Lambda)_{c.m.}$; the solid curves (sum of $\Lambda\pi^0$ and $\Sigma^0\pi^0$) are generated from the fitted coefficients and the missing-mass-squared resolution function, for the angular bins shown.

to find the expectation values of

$$\beta f_Y(\cos\theta, \mathfrak{M}) \sin\theta \frac{dP_l(\cos\theta)}{d(\cos\theta)},$$

where $\hat{n} = (\hat{K}^- \times \hat{\pi}^0)/|\hat{K}^- \times \hat{\pi}^0|$, $\mathbf{P}$ is the polarization of the observed $\Lambda$, and $\beta = \hat{p}_{\text{proton}} \cdot \hat{n}$.

Weighted histograms of $\beta$, for all events from the higher-momentum film in the $390 \pm 10$ MeV/$c$-momentum bin, are compared with the fitted curves in Fig. 8(a). Figure 8(b) shows the fitted polarizations, times the $\Lambda$ asymmetry parameter $\alpha$, for the observed $\Lambda$'s from the separate $\Lambda\pi^0$ and $\Sigma\pi^0$ channels. Measured polarizations from samples with strict $\mathfrak{M}$ cuts (0.008–0.018 BeV$^2$ for $\Lambda$'s and 0.044–0.070 BeV$^2$ for $\Sigma$'s) are plotted with the fitted polarization curves. The relationship of the $B_l^\Sigma$ to the $b_l^\Sigma$ is similar to that of the $A_l^\Sigma$ to the $a_l^\Sigma$, but since the $b_l^\Sigma$ are small and poorly determined, these $l$-dependent effects have not been calculated. For a $\Sigma^0$ with a given direction and polarization, the observed $\Lambda$ polarization (averaged over the $\Lambda$-$\Sigma$ angle, or equivalently over $\mathfrak{M}$) is $\mathbf{P}_\Lambda = -\frac{1}{3}\mathbf{P}_{\Sigma^0}$ for our $\mathfrak{M}$ cut.

The shape and relative amount of the recently reported[15] $\Lambda(1520) \to \Lambda\gamma$ and the shape and relative amount of the $\Sigma\gamma$ mode which the $\Lambda\gamma$ branching ratio and $SU_3$ invariance imply are shown in Fig. 9. No correction has been made for the presence of these modes in the calculation of the Legendre coefficients. A rough estimate of the contamination in the $\Lambda$ co-

[15] T. S. Mast, M. Alston-Garnjost, R. O. Bangerter, A. Barbaro-Galtieri, L. K. Gershwin, F. T. Solmitz, and R. D. Tripp, Phys. Rev. Letters **21**, 1715 (1968).

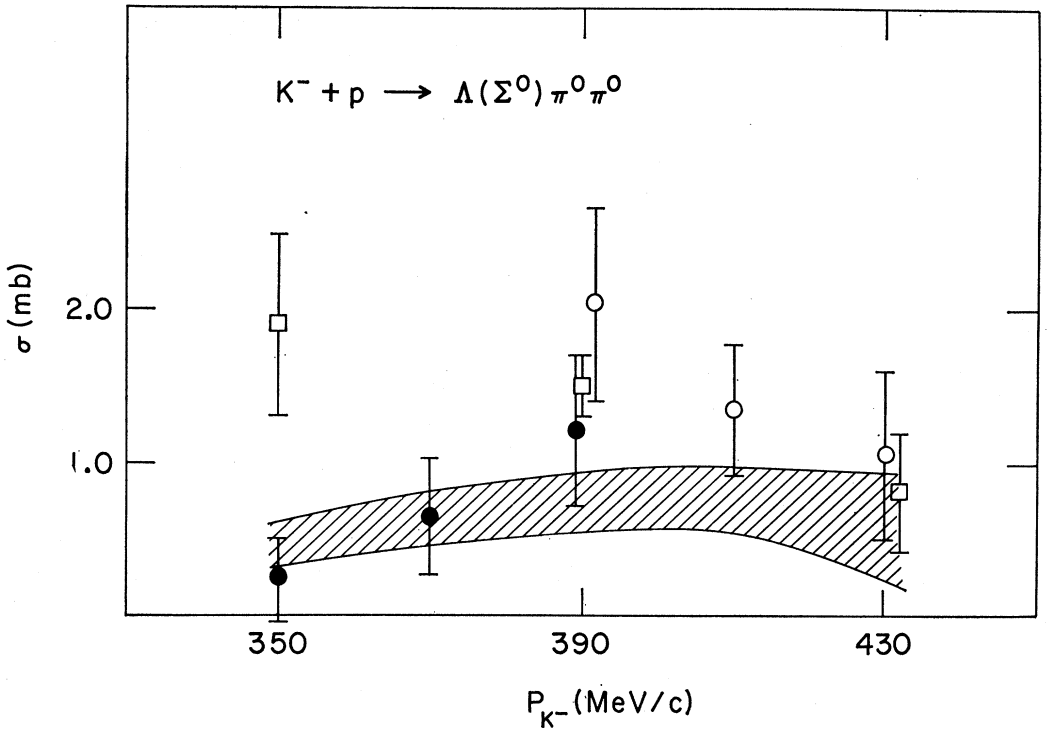


FIG. 7. Three-body ($\Lambda\pi^0\pi^0$ and $\Sigma^0\pi^0\pi^0$) cross sections. The open boxes are $\Lambda\pi^0\pi^0$ cross sections from Ref. 7. The solid circles are ($\Lambda\pi^0\pi^0+\Sigma^0\pi^0\pi^0$) cross sections from the lower-momentum film of this experiment, and the open circles are the corresponding cross sections from the higher-momentum film. The shaded area corresponds to $\frac{1}{2}\sigma(\Lambda\pi^+\pi^-)$ (the maximum $\Lambda\pi^0\pi^0$ cross section allowed by charge independence) from Ref. 7, with the errors quoted there.

efficients can be made from

$$C_{\Lambda\gamma}=\int d\mathfrak{M}\, f_\Lambda f_{\Lambda\gamma}\Big/\int d\mathfrak{M}\, f_\Lambda{}^2=\exp[-(m_{\pi^0}{}^2/2\sigma)^2]$$

$$\times\int(2\pi)^{-1/2}e^{-x^2/2}dx\cong\exp[-(m_{\pi^0}{}^2/2\sigma)^2].$$

The quantity $C_{\Lambda\gamma}$ times the ratio of the $\Lambda\gamma$ cross section to the $\Lambda\pi$ cross section ranges from 0.001 to 0.085 for different angle bins. The $\Sigma\gamma$ contamination can be computed similarly. These contaminations cause Legendre-coefficient distortions smaller than the errors.

The error matrix for the coefficients is found by propagating the statistical error matrix for the moments, using the matrix **C** which relates the moments **Q** to the $A_l{}^\Lambda$ and $a_l{}^\Sigma$. The error matrix for the $A_l{}^\Lambda$ and $A_l{}^\Sigma$ is then found from that for the $A_l{}^\Lambda$ and $a_l{}^\Sigma$ by appropriate multiplication by factors depending on $l$, $l'$. This error matrix has important off-diagonal elements, including those which correlate the $A_l{}^\Lambda$ with the $A_l{}^\Sigma$.

Because of the difficulty of separating the $\Lambda$'s and $\Sigma$'s, and because of uncertainties in normalization, we choose to display our results as cross sections ($A_0$) and angular shapes (the ratios $A_l/A_0$) separately. The variance matrix $\mathbf{S}_R$ for these ratios may be found from the variance matrix $\mathbf{S}_A$ for the $A_l{}^0$. We first note that

$$\delta\left(\frac{A_l{}^Y}{A_0{}^Y}\right)=\frac{\delta A_l{}^Y}{A_0{}^Y}-\frac{A_l{}^Y}{(A_0{}^Y)^2}\delta A_0{}^Y.$$

From this relation it follows that

$$S_{Rl^Ym^{Y'}}=\langle\delta(A_l{}^Y/A_0{}^Y)\delta(A_m{}^{Y'}/A_0{}^{Y'})\rangle=\frac{\langle\delta A_l{}^Y\delta A_m{}^{Y'}\rangle}{A_0{}^YA_0{}^{Y'}}-\frac{\langle\delta A_l{}^Y\delta A_0{}^{Y'}\rangle A_m{}^{Y'}}{A_0{}^Y(A_0{}^{Y'})^2}-\frac{A_l{}^Y\langle\delta A_m{}^Y\delta A_0{}^Y\rangle}{A_0{}^{Y'}(A_0{}^Y)^2}+\frac{A_l{}^YA_m{}^{Y'}\langle\delta A_0{}^Y\delta A_0{}^{Y'}\rangle}{(A_0{}^Y)^2(A_0{}^{Y'})^2}$$

$$=\left(S_{Al^Ym^{Y'}}-\frac{A_m{}^{Y'}}{A_0{}^{Y'}}S_{Al^Y0^{Y'}}-\frac{A_l{}^Y}{A_0{}^Y}S_{Am^{Y'}0^Y}+\frac{A_l{}^YA_m{}^{Y'}}{A_0{}^YA_0{}^{Y'}}S_{A0^Y0^{Y'}}\right)\Big/A_0{}^YA_0{}^{Y'},$$

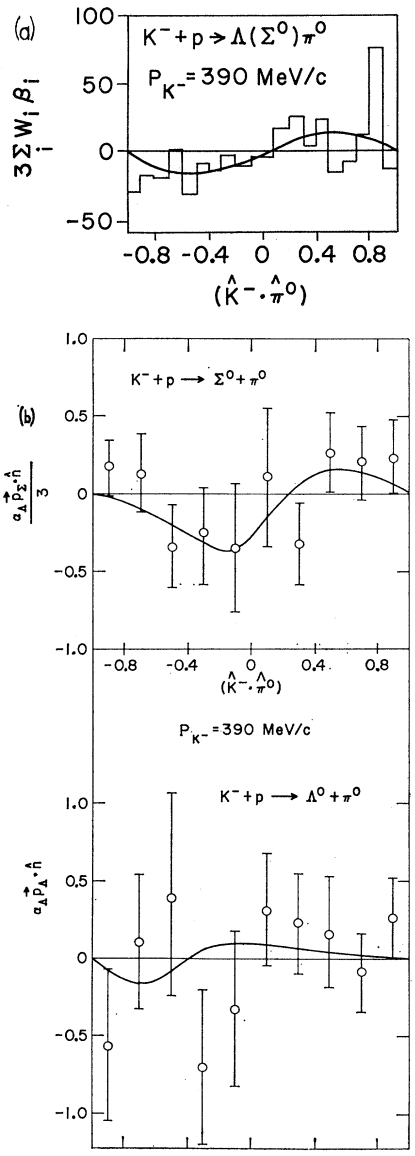


FIG. 8. (a) For the events in Fig. 4 below the $\Sigma^0\pi^0$ missing-mass-squared spectrum midpoint, the weighted distribution of $\beta = (\text{prôton} \cdot \hat{n})$, where $\hat{n} = (\hat{K}^- \times \hat{\pi}^0)/|\hat{K}^- \times \hat{\pi}^0|$, is shown. The smooth curve is generated from the fitted coefficients. (b) $\Lambda\pi^0$ and $\Sigma^0\pi^0$ polarizations are measured ($3\langle\beta\rangle$) for events in the missing-mass-squared cuts 0.008–0.018 BeV$^2$ for $\Lambda\pi^0$ and 0.044–0.070 BeV$^2$ for $\Sigma^0\pi^0$. The solid curves are generated for the pure $\Lambda\pi^0$ and $\Sigma^0\pi^0$ cases from the fitted coefficients.

where the index $V$ ranges from 1 to 2 for the $\Lambda$-$\Sigma^0$ error matrix and is equal to 1 only for the $\bar{K}^0$ error matrix. To include the effects of correlations, the full error matrix is used in the partial-wave analysis described in Sec. IV.

Various possible systematic errors have been considered, including (1) effects of the manner of averaging the measured $K^-$ momentum value with information from the beam momentum distribution, (2) changes due to the uncertainty in the missing-mass resolution function, and (3) angle errors due to lack of coincidence of the last bubble on the $K^-$ and the true end of the track. These systematic effects led to differences in the coefficients of the order of the errors. Where necessary, the Legendre-coefficient errors quoted were increased to reflect these systematic errors. The diagonal terms of the error matrices are also increased; this will cause a small underestimation of the correlations. The final Legendre coefficients are shown in Figs. 10 and 11 and in Table II. These systematic effects are discussed in detail in the three following paragraphs.

(1) Wrongly assigned $K^-$ momenta may cause the mean momentum of the events in a given momentum bin to be incorrectly estimated. For very short tracks the mean value of the beam momentum is a better estimate of the true momentum than is measured momentum; for longer tracks, the reverse is usually true. We have computed the coefficients using an error-weighted average of the measured beam momentum and the central beam momentum, and also using the measured momentum only. For our momentum bins, 20 MeV/$c$ wide, the mean measured momentum may differ from the "beam-averaged" momentum by 5–10 MeV/$c$. This difference is a measure of the uncertainty in the momentum assigned to our Legendre-coefficient measurements. (A wrong incident $K^-$ momentum may also cause an individual event to be put in a wrong momentum bin, leading to correlations between different bins. This effect is discussed with the normalization at the end of this section.)

(2) The missing-mass resolution function determines the width, at various production angles, of the Gaussians which describe the missing-mass-squared distribution. Various widths have been tried, and that width which best fits the overall $\mathfrak{M}$ distribution has been used. Changes in the resolution function affect cross-section determinations more than the coefficient ratios.

(3) Taking the last visible bubble as the end of the $K^-$ track may introduce errors in the $V^0$ production angle and momentum; for the $\Lambda$'s these errors are particularly serious since the angle and momentum errors propagate into the missing mass squared, which is used in the $\Lambda$-$\Sigma$ separation. A small sample of events was processed through geometry and kinematics with and without adding an average observed $K^-$ "bubble gap length" of 200 $\mu$ to the end of the track, and corrections were estimated from the results. The effect is greatest for the $\Lambda$-$\Sigma$ cross sections. It was found that this observed effect was well reproduced by a shift of $\mathfrak{M} \to \mathfrak{M} - 0.1(m_{\pi^0})^2$ in the missing-mass-squared scale. (This corresponds to redefining the endpoints of the $\Sigma^0\pi^0$ spectrum and the position of the ideal spike for $\Lambda\pi^0$ events missing mass squared.) This shift has been applied to the experimental missing-mass-squared histograms in Figs. 4 and 6.

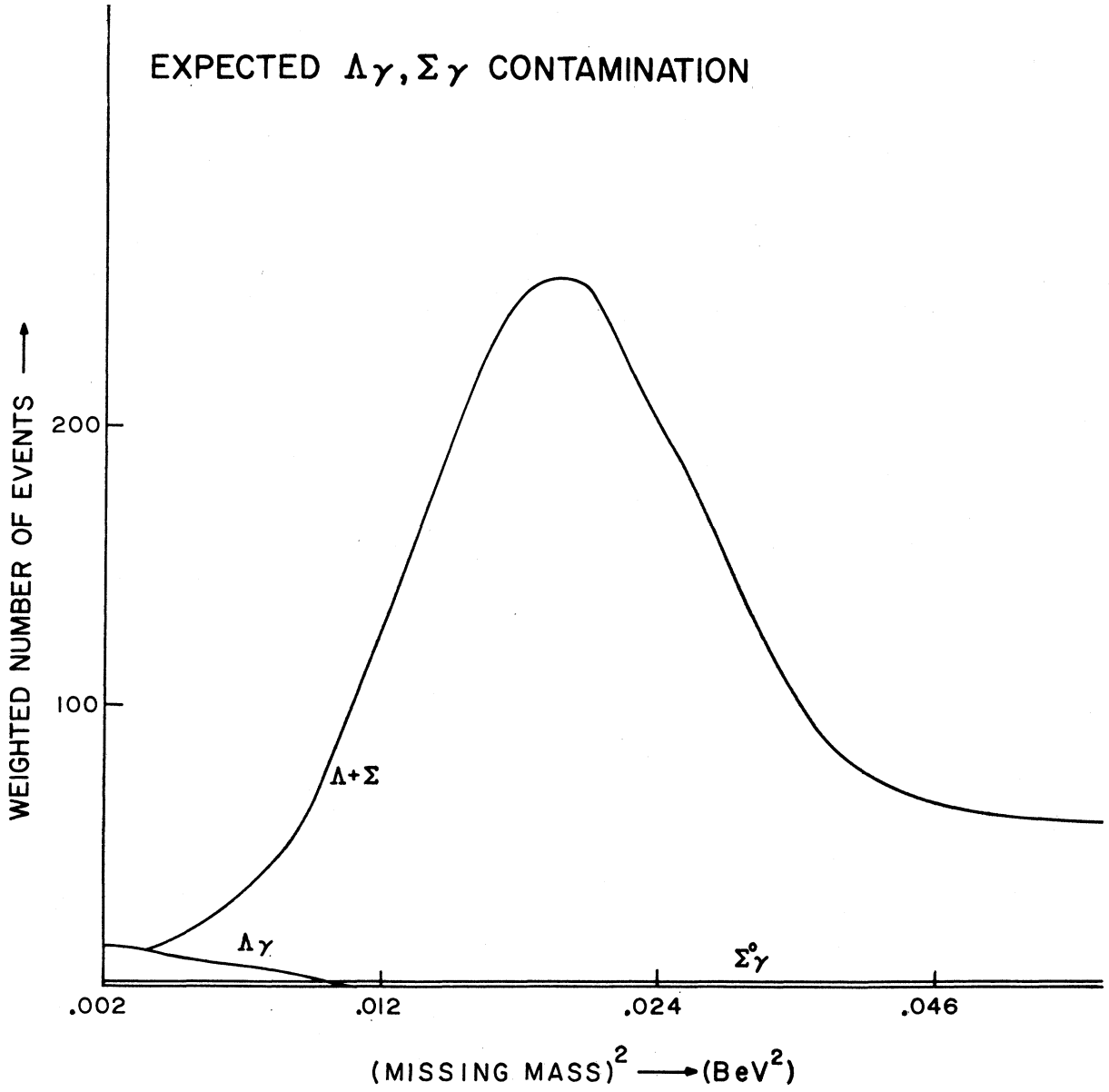


FIG. 9. Expected missing mass squared for the decay $\Lambda(1520) \to \Lambda\gamma$, $\Sigma\gamma$, relative to $\Lambda(1520) \to \Lambda\pi^0$.

The $K^-$ beam flux was obtained by studying a partly measured sample of scanned $K^- \to \pi^+\pi^-\pi^-$ ($\tau$) decays in the same fiducial volume.[16] The average number of $K^-$ times the average time they spend in the chamber, needed for the cross-section determination, is found by averaging the instantaneous equation for $\tau$ decay over the fiducial volume and momentum bin:

$$dN_\tau/dt = (1/\tau_\tau)N_{K^-}. \quad (2)$$

Averaging (2), we find

$$(\text{number of } \tau\text{'s seen})/\langle \Delta t \rangle = (1/\tau_\tau)\langle N_{K^-} \rangle,$$
$$(\text{number of } \tau\text{'s seen})\tau_\tau = (\Delta t)\langle N_{K^-} \rangle,$$

where $\tau_\tau$ is the partial $K^-$ lifetime into the $\tau$ mode. Except for a velocity factor, then, the pathlength used to determine the beam flux is equal to the number of $\tau$'s times the $\tau_\tau$. Note that determining the average effective pathlength in this way automatically corrects for attenuation of the $K^-$ beam through interactions in the chamber. The cross sections are shown in Table II, and Table III gives the pathlength distribution derived from the $\tau$'s, expressed as events/mb. Table III

[16] The $\tau$ events used were provided by P. Lucas from measurements on the Yale PEPR system, which has been described by V. D. Bogert, in Proceedings of the International Colloquium on PEPR, Nijmegen, Netherlands, 1968 (unpublished). The geometry program used for the $\tau$'s was TVGP.

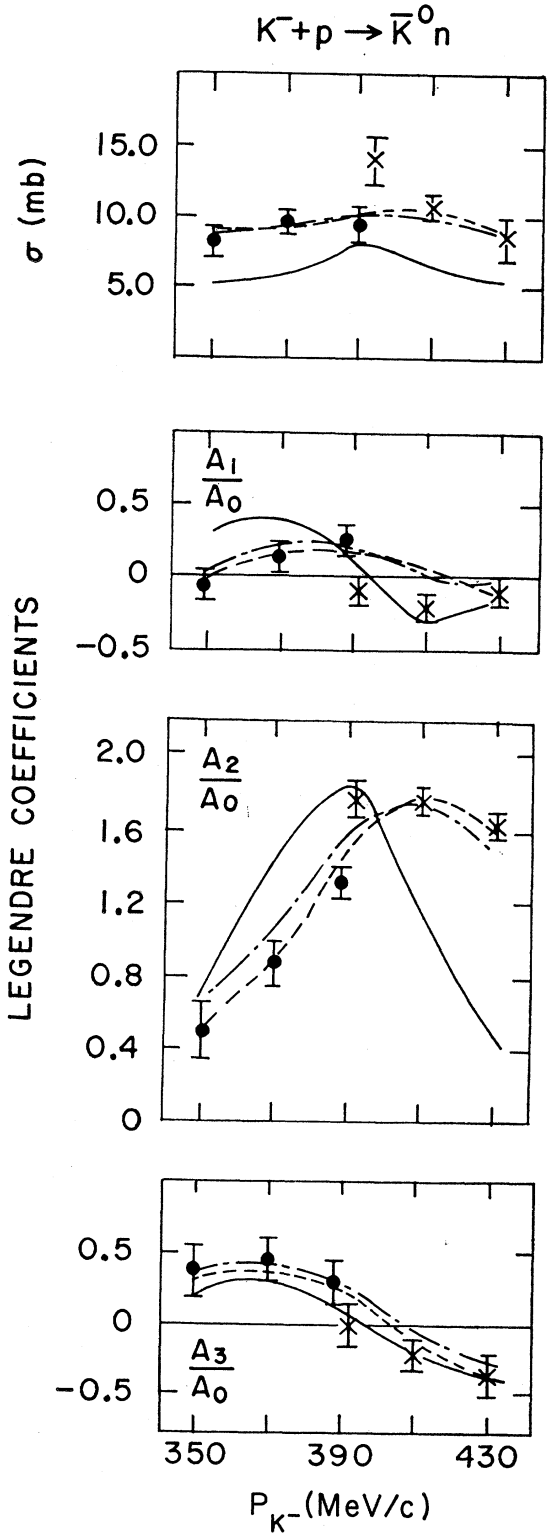


FIG. 10. Cross sections and angular distribution Legendre coefficients for the $\bar{K}^0 n$ channel. Momentum errors are of the order of 5 MeV/$c$. The closed circles are data from momentum bins of the low-$P_{K^-}$ film; the ×'s are from the higher-momentum film. The solid lines are the predictions from the fit of Kim (Ref. 19); the dot-dashed lines are from the effective-range fit of this experiment; and the dashed lines are from the constant $K$-matrix fit of this experiment. The small $A_3$ and $B_3$ measured coefficients are not shown.

also gives the number of events involved in determining the cross sections and Legendre-coefficient ratios; only events from film with available $\tau$ scanning were used to determine the cross sections.

Some discrepancies exist for the cross sections from the overlap region between the higher- and lower-momentum film. These discrepancies may be attributed in part to the uncertainties, included in the systematic-error discussion above, of 5–10 MeV/$c$ in the mean momentum of events in one momentum bin. They may also be attributed in part to the fact that different geometry programs were used to process the $NV$ (NP-54) and $\tau$ (TVGP) events. Since the two programs use slightly different procedures to fit the measured points to "measured" angles and momenta, the resulting distributions may have somewhat different shapes. In particular, the distributions of $\delta P_{K^-}$, the error in the "measured" $K^-$ momentum, are noticeably different for the two cases, with a peak at larger $\delta P_{K^-}$ for the $\tau$'s than for the $NV$'s. If this reflects only a difference in the geometry programs, then the $\tau$ momentum distribution obtained by averaging the measured beam momentum with the central beam value will be relatively narrower than that same distribution for the $NV$'s, leading to systematic errors in the cross section. Cross sections have been computed using the measured and the averaged beam momenta. The average of the two methods is reported, but in the overlap bin at 390 MeV/$c$ the cross sections from the measured momenta are more consistent than those from the averaged momenta.

Even if the same geometry programs were used to obtain the $\tau$ and $NV$ momenta, wrong beam-track measurements may still cause events to be placed in wrong bins or may bias the mean momentum of a given bin, as is mentioned in the discussion of systematic effects in the Legendre coefficients. $K^-$ momentum uncertainties are comparable to the size of the momentum bins used, and these problems cause discontinuities in the rapidly varying quantities at the 390-MeV/$c$ bin where the two runs overlap.

For the Legendre-coefficient ratios, which relate to the shape of the angular distributions, statistical correlations between the different ratios, but not between different momentum bins, are included in the coefficient error matrix. For the cross sections, however, correlations between different momentum bins are included, for both $NV$'s and $\tau$'s.[17]

## IV. PARTIAL-WAVE ANALYSIS

The amplitudes used fall into three categories: (1) the resonant $\Lambda(1520)$ isospin-0 $D_{3/2}$ wave, (2) the small

[17] M. Sakitt, thesis, University of Maryland Technical Report No. 410, 1961 (unpublished).

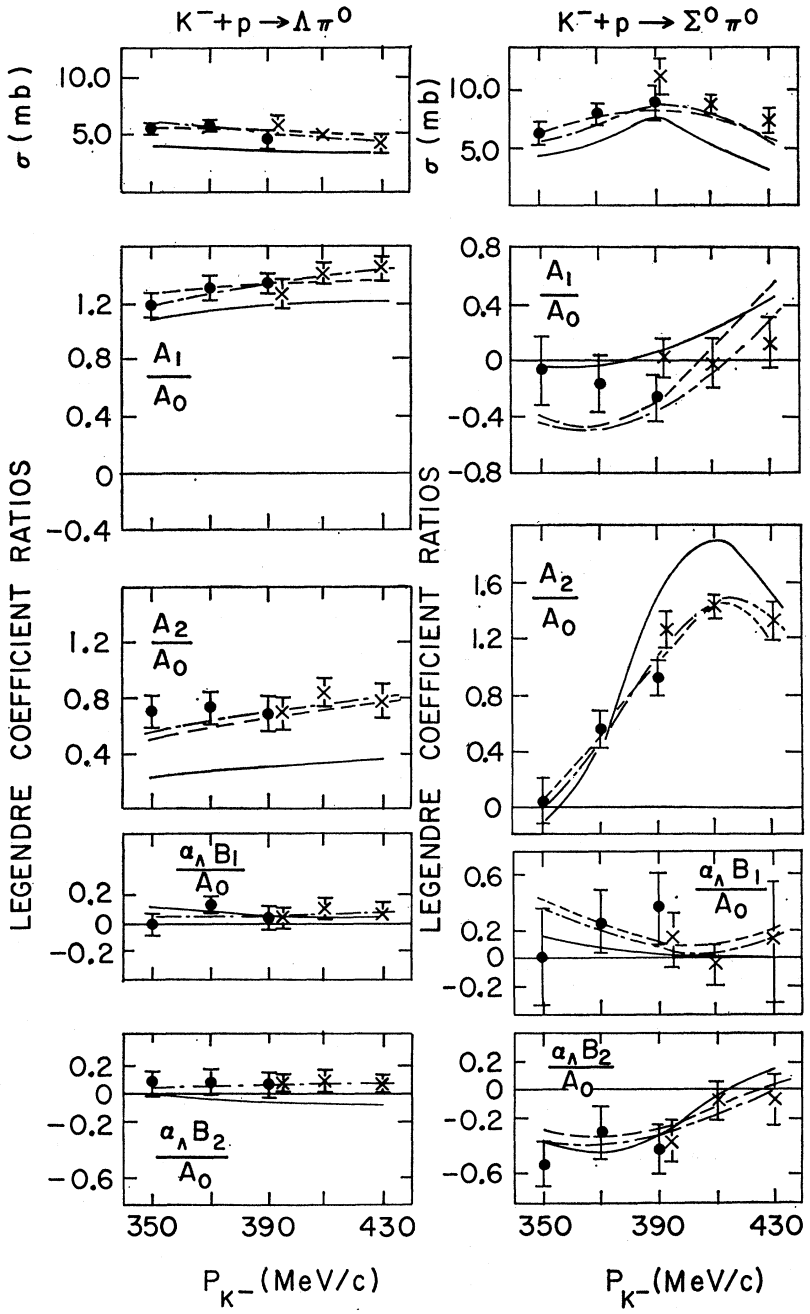


FIG. 11. Cross sections, angular distribution Legendre coefficients, and polarization Legendre coefficients muliplied by the $\Lambda$-decay asymmetry parameter for the $\Lambda\pi^0$ and $\Sigma^0\pi^0$ channels. The meaning of the symbols is the same as in Fig. 10.

isospin-1 $D_{3/2}$ wave, and (3) the quite appreciable $S$, $P_{1/2}$, and $P_{3/2}$ waves. Two different methods have been used to describe these $S$ and $P$ waves: (a) a constant-$K$-matrix formalism, and (b) a $K$ matrix which is explicitly momentum-dependent through the introduction of effective ranges. A $K$-matrix formalism could have been used for the background isospin-1 $D_{3/2}$ wave as well. However, it is quite small and for convenience and ease of comparison with previous fitting in this region, we have chosen a constant-scattering-length formalism.

We describe below the partial-wave amplitude parametrization in detail.

(1) A Breit-Wigner resonant amplitude with energy-dependent width has been used to characterize the $\Lambda(1520)$ resonance: If $T_{ij}'(l,J,I)$ is the isospin $I$ amplitude for the transition $i \to j$ with orbital and total angular momenta $l$ and $J$, respectively, then $T_{ij}'(2,\frac{3}{2},0) \equiv D_{03} = (\Gamma_i\Gamma_j/\Gamma_R^2)^{1/2}/(\epsilon - i)$, where $\epsilon = 2(E_R - E)/\Gamma(E)$, $\Gamma(E)$ varies as $k/(1+x^2/k^2)^2$, $\Gamma(E_R) = \Gamma_R$, and $k$ = the $K^-p$ center-of-mass momentum in units of $\hbar$.

TABLE II. Neutral-channel Legendre coefficients, $K^-+p$ interactions near 400 MeV/$c$.

| $P_{K^-}$ (MeV/$c$) | $\sigma$ (mb) | $A_1/A_0$ | $A_2/A_0$ | $A_3/A_0$ | $\alpha_\Lambda B_1/A_0$ | $\alpha_\Lambda B_2/A_0$ | $\alpha_\Lambda B_3/A_0$ |
|---|---|---|---|---|---|---|---|
| | | | | $\Lambda\pi^0$ coefficients | | | |
| 350 | 5.6±0.7 | 1.19±0.08 | 0.71±0.11 | 0.01±0.08 | −0.01±0.08 | 0.07±0.07 | −0.04±0.07 |
| 370 | 5.7±0.6 | 1.31±0.07 | 0.74±0.13 | 0.20±0.17 | 0.13±0.06 | 0.08±0.07 | −0.04±0.06 |
| 390 | 4.5±0.7 | 1.32±0.09 | 0.69±0.14 | 0.02±0.20 | 0.02±0.09 | 0.06±0.09 | −0.06±0.08 |
| 390 | 5.7±0.6 | 1.25±0.08 | 0.66±0.11 | −0.10±0.19 | 0.05±0.08 | 0.05±0.07 | 0.0 ±0.06 |
| 410 | 4.8±0.5 | 1.45±0.06 | 0.86±0.10 | 0.23±0.13 | 0.10±0.06 | 0.13±0.05 | 0.06±0.05 |
| 430 | 4.2±0.6 | 1.47±0.08 | 0.77±0.12 | 0.26±0.15 | 0.08±0.09 | 0.06±0.07 | 0.06±0.07 |
| | | | | | $-\alpha_\Lambda B_1/3A_0$ | $-\alpha_\Lambda B_2/3A_0$ | $-\alpha_\Lambda B_3/3A_0$ |
| | | | | $\Sigma^0\pi^0$ coefficients | | | |
| 350 | 6.2±0.7 | −0.09±0.24 | 0.05±0.17 | 0.28±0.22 | −0.01±0.11 | 0.18±0.09 | −0.08±0.08 |
| 370 | 8.1±0.8 | −0.17±0.22 | 0.55±0.13 | 0.09±0.16 | −0.09±0.08 | 0.10±0.06 | −0.04±0.05 |
| 390 | 9.1±1.3 | −0.26±0.17 | 0.91±0.12 | 0.17±0.14 | −0.13±0.08 | 0.14±0.07 | −0.02±0.05 |
| 390 | 11.6±1.7 | 0.02±0.15 | 1.26±0.14 | 0.06±0.14 | −0.05±0.06 | 0.13±0.05 | −0.05±0.06 |
| 410 | 8.8±0.9 | −0.02±0.17 | 1.44±0.10 | −0.20±0.11 | 0.01±0.05 | 0.02±0.05 | 0.01±0.05 |
| 430 | 7.5±1.0 | 0.13±0.19 | 1.32±0.14 | −0.13±0.18 | −0.03±0.14 | 0.02±0.07 | −0.03±0.14 |
| | | | | $\bar{K}^0n$ coefficients | | | |
| 350 | 8.0±0.7 | −0.08±0.10 | 0.53±0.16 | 0.37±0.15 | | | |
| 370 | 9.6±0.7 | 0.15±0.11 | 0.91±0.11 | 0.45±0.13 | | | |
| 390 | 9.3±1.0 | 0.27±0.13 | 1.33±0.09 | 0.33±0.13 | | | |
| 390 | 14.0±1.7 | −0.13±0.12 | 1.79±0.08 | −0.03±0.13 | | | |
| 410 | 10.6±0.9 | −0.20±0.09 | 1.78±0.07 | −0.24±0.11 | | | |
| 430 | 8.4±1.3 | −0.15±0.11 | 1.64±0.09 | −0.39±0.12 | | | |

TABLE III. Events used to determine Legendre coefficients and cross sections.

| Momentum bin | Observed Λ's (cut) Legendre coeff. | $\sigma$ | Observed $\bar{K}^0$'s (cut) Legendre coeff. | $\sigma$ | Events/mb |
|---|---|---|---|---|---|
| 350 | 1331 | 974 | 658 | 499 | 265 |
| 370 | 2029 | 1500 | 1084 | 815 | 349 |
| 390 | 2052 | 1508 | 1192 | 870 | 400 |
| 390 | 1990 | 1355 | 1097 | 860 | 258 |
| 410 | 3287 | 2240 | 1792 | 1342 | 547 |
| 430 | 3117 | 2110 | 1480 | 1103 | 650 |

TABLE IV. Parameters of effective-range fit. $M_{AB}{}^I$ is the $M$ matrix element (in fm$^{-(2l+1)}$) and $r_A{}^I$ is the diagonal range (in fm) for the isospin $I$ transition from channel $A$ to channel $B$. $a$ and $b$ (in fm$^5$) are the real and imaginary parts of the $D_{13}$ scattering length, $\epsilon_\Sigma$ is the ratio $\sigma_{(\Sigma\pi)}/(\sigma_{(\Sigma\pi)}+\sigma_{(\Lambda\pi\pi)})$ for the $D_{13}$ transition, and $\varphi_\Sigma$ (in radians) is the phase angle for $D_{13}{}^{\Sigma\pi}$. The widths $\Gamma$ and center-of-mass energy $E_R$ of the resonance are in MeV, and $x^2$ (in fm$^{-2}$) is the square of the inverse of the interaction radius. The errors quoted are the variable change necessary to change the $\chi^2$ by 1.

| | $S$ | $P_{1/2}$ | $P_{3/2}$ | | $D_{3/2}$ |
|---|---|---|---|---|---|
| Isospin 0 | | | | Isospin 0 | |
| $M_{KK}{}^0$ | 0.03±0.03 | −4.43±0.60 | 7.96±0.40 | $E_R$ | 1521.6±0.4 |
| $M_{K\Sigma}{}^0$ | −1.50±0.03 | −8.32±0.23 | −2.97±0.43 | $\Gamma_R$ | 26.9±0.7 |
| $M_{\Sigma\Sigma}{}^0$ | 2.61±0.09 | −4.17±0.35 | 15.70±3.0 | $\Gamma_K$ | 8.0±0.12 |
| $r_K{}^0$ | 0.23±0.04 | | | $\Gamma_\Sigma$ | 17.3±0.8 |
| $r_\Sigma{}^0$ | 1.26±0.40 | | | $x^2$ | 0.0±0.4 |
| Isospin 1 | | | | Isospin 1 | |
| $M_{KK}{}^1$ | −4.34±0.09 | −14.64±1.05 | −21.90±0.14 | $a$ | 0.005 ±0.004 |
| $M_{K\Sigma}{}^1$ | −4.88±0.04 | 6.72±0.70 | −65.30±1.0 | $b$ | 0.0002±0.0001 |
| $M_{K\Lambda}{}^1$ | 0.91±0.05 | 2.90±1.10 | −12.99±0.44 | $\epsilon_\Sigma$ | 1.0 ±0.06 |
| $M_{\Sigma\Sigma}{}^1$ | −2.98±0.06 | −2.80±0.60 | −122.3 ±4.0 | $\varphi_\Sigma$ | −4.41 ±0.70 |
| $M_{\Sigma\Lambda}{}^1$ | 1.75±0.06 | −11.49±0.97 | −7.0 ±1.5 | | |
| $M_{\Lambda\Lambda}{}^1$ | 0.22±0.06 | −14.05±2.90 | −2.8 ±0.4 | | |
| $r_K{}^1$ | −3.26±0.20 | | −0.52±0.10 | | |
| $r_\Sigma{}^1$ | 0.93±0.30 | | 0.7 ±2.1 | | |
| $r_\Lambda{}^1$ | −0.60±0.24 | | 0.40±0.04 | | |

TABLE V. $\chi^2$ contributions.

| No. of data | Source | $\chi^2$ contributions effective-range fit (120 degrees of freedom 44 parameters) | Constant $K$-matrix fit (128 degrees of freedom 36 parameters) |
|---|---|---|---|
| 18 | $\bar{K}^0n$ Legendre-coefficient ratios | 34.3 | 31.9 |
| 72 | $\Lambda\pi^0$ and $\Sigma^0\pi^0$ Legendre-coefficient ratios | 56.6 | 60.6 |
| 18 | $\bar{K}^0n$, $\Lambda\pi^0$, and $\Sigma^0\pi^0$ cross sections | 43.3 | 37.9 |
| 36 | $K^-p$, $\Sigma^-\pi^+$, $\Sigma^+\pi^-$ Legendre-coefficients (Ref. 7) | 54.5 | 21.7 |
| 20 | Measured $\alpha$ **P** for $\Sigma^+\pi^-$ channel (Ref. 8) | 20.8 | 44.5 |
| 164 | | 209.5 | 196.6 |

(2) The small isospin-1 $D_{3/2}$ background amplitude has been parametrized with a constant-scattering-length formalism: $D_{13}^{\bar{K}N}=k^5A/(1-ik^5A)$ and $D_{13}^{\Sigma\pi}=e^{i\varphi_\Sigma}\{k^5b\epsilon_\Sigma/[(1+k^5b)^2+(k^5a)^2]\}^{1/2}$, where $A=a+ib$ is the complex constant scattering length, $\epsilon_\Sigma$ is the branching ratio into the $\Sigma\pi$ channel, and $\varphi_\Sigma$ is the phase of the $\Sigma\pi$ amplitude.

(3) A $K$-matrix formalism has been used for the background $S$, $P_{1/2}$, and $P_{3/2}$ waves. For these background amplitudes two different assumptions about the $K$ matrix have been used.

(a) A constant $K$ matrix with the parametrization recently used by Martin and Sakitt[18] to fit $K^-p$ amplitudes in the range 0–300 MeV/$c$: $T_{ij}'(l,J,I)=(K'^{-1}-i)^{-1}=\rho^{1/2}(K^{-1}-ip)^{-1}\rho^{1/2}$, where $K$ is the $K$ matrix of Dalitz and Tuan[9] and $\rho$ is a phase-space density matrix; $\rho_{ij}=k_i^{(2l+1)}$ for $i=j$ and $\rho_{ij}=0$ for $i\neq j$.

(b) The second method for parametrizing these background waves is a momentum-dependent $K$ matrix, using two terms in the effective-range expansion of Ross and Shaw. In this case, $K^{-1}$ is expanded about some energy $E_0$ in terms of a constant matrix $M$ and effective ranges $r_i$:

$$\begin{aligned}(K^{-1})_{ij}&=M_{ij}\quad\text{for}\quad i\neq j\\&=M_{ii}-\tfrac{1}{2}C_l r_i^{-2l+1}\{k_i^2(E)-k_i^2(E_0)\\&\quad+\tfrac{1}{2}e_l r_i^2[k_i^4(E)-k_i^4(E_0)]+\cdots\}\\&\qquad+\text{small residual term}\quad\text{for}\quad i=j,\end{aligned}$$

where $C_0=-1$, $C_1=3$, $e_0=\frac{1}{3}$, and $e_1=-\frac{1}{3}$. Kim has previously fitted $K^-p$ amplitudes from 0 to 550 MeV/$c$, using one term in this expansion.[19]

The isospin pure waves are combined according to Clebsch-Gordan coefficients to give the amplitudes $T(l,J)$ for the physical channels. These amplitudes are then related to the differential cross section $I$ and the product $I\mathbf{P}$ of $I$ with the polarization by the equations

$$I=|f|^2+|g|^2\quad\text{and}\quad I\mathbf{P}=2\,\mathrm{Re}(f^*g)\hat{n},$$

where

$$f(\theta)=[(4\pi)^{1/2}/k]\sum_l(2l+1)^{-1/2}\times[(l+1)T(l,l+\tfrac{1}{2})+lT(l,l-\tfrac{1}{2})]Y_l^0$$

and

$$g(\theta)=\frac{i(4\pi)^{1/2}\sin\theta}{k}\sum_l(2l+1)^{-1/2}\times[T(l,l+\tfrac{1}{2})-T(l,l-\tfrac{1}{2})]\frac{d}{d\cos\theta}Y_l^0(\theta).$$

Because the $K$ matrix couples the various channels and requires many parameters, it is desirable to have input data for as many channels as possible. Therefore, published data on the $K^-p$, $\Sigma^-\pi^+$, and $\Sigma^+\pi^-$ channels in this region[7,8] have been included in the fitting.

The program MINFUN[20] was used to obtain a set of partial-wave parameters which fit the observed angular distributions and polarizations. Although no energy continuity with other data is demanded, Kim's parameters are used as a starting point for the momentum-dependent $K$-matrix assumption, and the parameters of Martin and Sakitt are used for the constant $K$-matrix assumption for the $S$ waves.[21] (Martin and Sakitt use only $S$ waves in their low-momentum region.) For each $K$-matrix assumption the final $S$ waves are similar to the input $S$ waves, which do fit the low-energy data. The other waves are small even in our higher-momentum region and do show some disagreements with Kim's input waves, as may be seen from the final waves in Figs. 12–14.

The initial momentum-dependent fitting was done with exactly the same parametrization as Kim's, and several solutions were found with similar $\chi^2$'s (about 225, with 120 degrees of freedom) and fitted curves.

[18] B. R. Martin and M. Sakitt, Phys. Rev. **183**, 1345 (1969).
[19] J. Kim, Phys. Rev. Letters **19**, 1074 (1967).
[20] A. Rosenfeld and W. Humphrey, Ann. Rev. Nucl. Sci. **13**, 103 (1963).
[21] The signs of initial values of $K_{K\text{-}\Sigma}{}^0$, $K_{K\text{-}\Sigma}{}^1$ and $K_{K\text{-}\Lambda}{}^1$ have been reversed from those of Martin and Sakitt (Ref. 18). This sign change leaves the $K$-nucleon amplitudes unchanged but rotates the hyperon amplitudes by 180°. The fitting of Martin and Sakitt does not discriminate between the two signs, but in our momentum region the interference with the $\Lambda(1520)$ $D_{3/}$ wave fixes the sign.

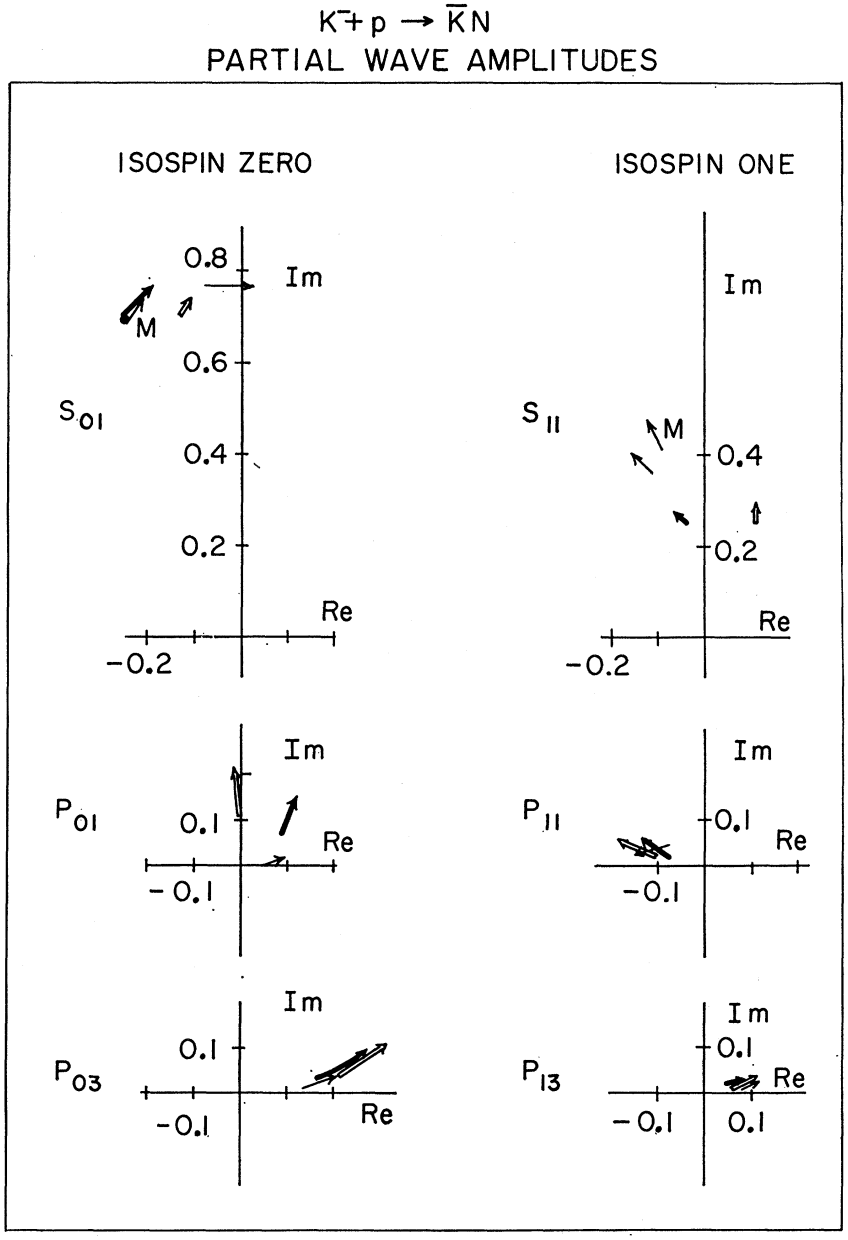


FIG. 12. $K^-+p\to\bar{K}N$ isospin amplitudes. The directed arrows (or heavy dots where the amplitudes change negligibly) begin at the amplitude value for 350 MeV/$c$ and end at the value for 430 MeV/$c$. The arrows accompanied by an $M$ are the $S$ waves of Ref. 18, and the thin arrows are the amplitudes of Ref. 19. The heavy arrows are the effective-range amplitudes from this experiment, and the double arrows are the constant $K$-matrix amplitudes from this experiment.

Of these, we picked the solution with the $S$ waves closest to those of Kim, and added the second term in the Ross and Shaw effective-range expansion; final minimizing then yielded a solution with a $\chi^2$ of 210. It is this solution with $k^4$ terms for which the parameters are shown in Table IV, with the $\chi^2$ contributions shown in Table V; no decrease in $\chi^2$ was found upon subsequently allowing $K^4$ terms in the other effective-range solutions.

The constant $K$-matrix parametrization, with eight more degrees of freedom than the effective-range formalism, yielded only one fit, a solution with a $\chi^2$ of 197, slightly lower than that of the effective-range fit. The $\chi^2$ contributions and the parameters for this solution are shown in Tables V and VI. The errors shown are the parameter change necessary to increase the $\chi^2$ by one. There are correlations among the parameters, particularly among those describing the same isospin angular-momentum wave, but no quantitative estimates of these correlations are made. A second caution concerns the errors for the position and widths of the $\Lambda(1520)$ Breit-Wigner resonant wave. Our determined parameters ($M_\Lambda=1521$ MeV, $\Gamma=26$–$27$ MeV, $\Gamma_K=7$–$8$ MeV, $\Gamma_\Sigma=14$–$17$ MeV, and the elasticity

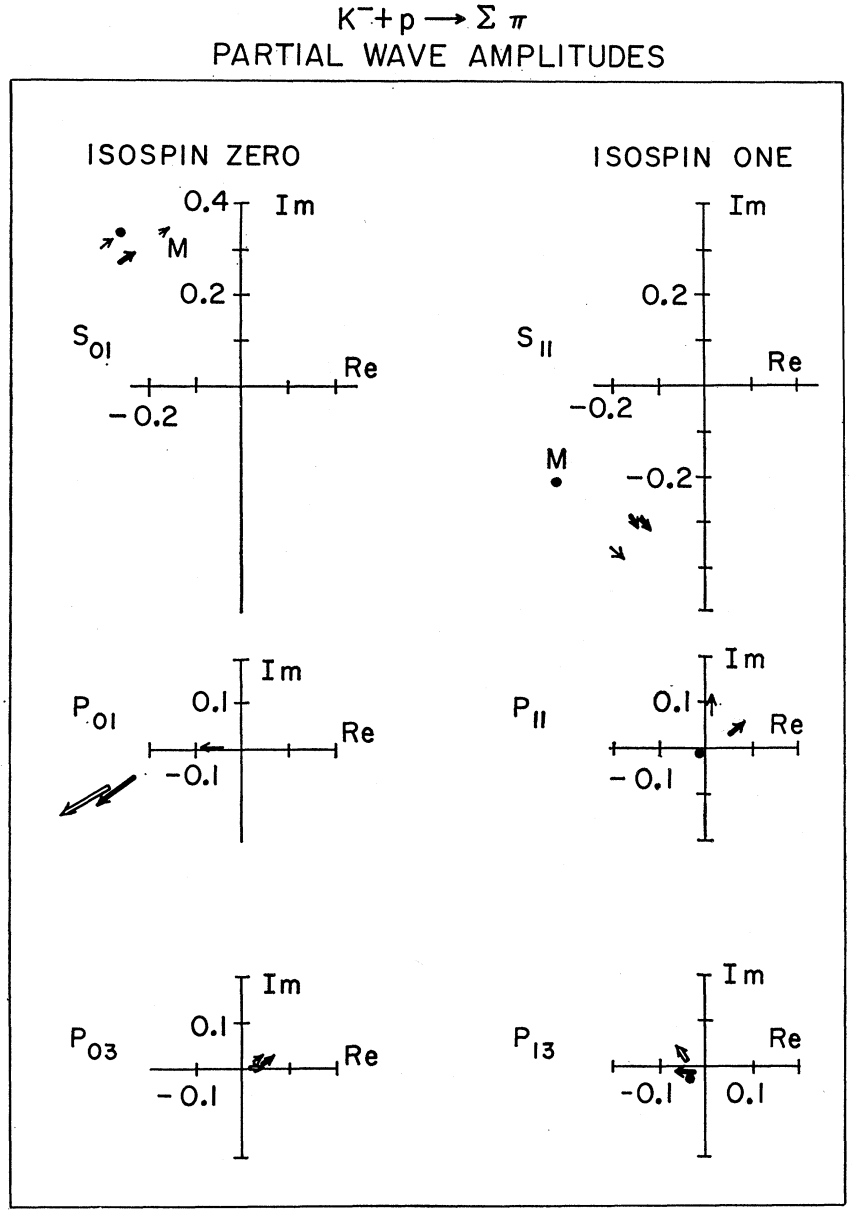


FIG. 13. $K^-+p \to \Sigma\pi$ isospin amplitudes. The meaning of the symbols is the same as in Fig. 12.

$\Gamma_K/\Gamma=0.25$–$0.3$) disagree with those found in other recent experiments.[22] The errors shown in Tables V and VI, determined from the $\chi^2$ change of 1, would make this disagreement appear significant. However, our momentum bins are 20 MeV/$c$ wide, with systematic central-value uncertainties of 5–10 MeV/$c$. These uncertainties are clearly displayed in the discrepancies in the overlapping bins at 390 MeV/$c$, between the low- and high-momentum film. This bin is near the peak of the resonance and the determination of the resonance parameters is quite sensitive to the 390-MeV/$c$ values. The real uncertainties in these parameters may be expected to be of the order of the central-value uncertainties; for example, approximately 5 MeV in the $\Lambda(1520)$ mass and about 30% in the widths.

Figures 11 and 12 compare the neutral-channel data from our experiment with the predictions of Kim's fit and of our two fits. There are several systematic disagreements between the Kim-fit predictions and our data and fit predictions, most noticeably in the cross sections and $A_2/A_0$ ratios. The $A_2/A_0$ disagreement is not too surprising since no detailed data on the angular structure of the neutral channels in these regions was available when Kim did his fitting. The cross-section discrepancies are more serious since Kim's amplitudes

[22] R. Levi Setti, Rapporteur talk in Proceedings of the Lund International Conference on Elementary Particles, Lund, Sweden, 1969 (unpublished).

TABLE VI. Parameters of constant $K$-matrix fit. $K_{AB}{}^{I}$ is the $K$-matrix element (dimensionless) for the isospin $I$ transition from channel $A$ to channel $B$. The remaining quantities are defined as in Table IV.

| | $S$ | $P_{1/2}$ | $P_{3/2}$ | | $D_{3/2}$ |
|---|---|---|---|---|---|
| Isospin 0 | | | | Isospin 0 | |
| $K_{KK}{}^{0}$ | −2.04±0.09 | 0.03 ±0.01 | 0.155±0.008 | $E_R$ | 1521.2±0.6 |
| $K_{K\Sigma}{}^{0}$ | −1.28±0.04 | −0.216±0.006 | 0.011±0.005 | $\Gamma_R$ | 26.0±0.8 |
| $K_{\Sigma\Sigma}{}^{0}$ | −0.40±0.04 | 0.13 ±0.03 | 0.10 ±0.20 | $\Gamma_K$ | 6.8±0.2 |
| | | | | $\Gamma_\Sigma$ | 14.0±0.4 |
| | | | | $x^2$ | 0.0±0.4 |
| Isospin 1 | | | | Isospin 1 | |
| $K_{KK}{}^{1}$ | 0.56±0.02 | −0.077±0.006 | 0.049±0.006 | $a$ | 0.014 ±0.002 |
| $K_{K\Sigma}{}^{1}$ | 0.66±0.02 | −0.007±0.008 | −0.029±0.006 | $b$ | 0.0001±0.0001 |
| $K_{K\Lambda}{}^{1}$ | 0.39±0.01 | −0.065±0.005 | −0.043±0.002 | $\epsilon_\Sigma$ | 1.0 ±1.0 |
| $K_{\Sigma\Sigma}{}^{1}$ | 1.07±0.05 | 0.010±0.20 | −0.248±0.090 | $\varphi_\Sigma$ | −5.84 ±0.70 |
| $K_{\Lambda\Sigma}{}^{1}$ | 0.10±0.02 | 0.02 ±0.05 | −0.054±0.020 | | |
| $K_{\Lambda\Lambda}{}^{1}$ | 0.50±0.03 | 0.19 ±0.02 | 0.046±0.010 | | |

did fit the previously available neutral two-body cross sections.[7] However, these previous cross sections were based on low statistics. The cross sections which we report are in better agreement with more recent cross sections,[22] though systematic differences in the $\Sigma^0\pi^0$ and $\Lambda\pi^0$ channels remain. These systematic differences are smaller than the differences with Kim's fit, and we attribute them to the difficulties of $\Lambda$-$\Sigma_i$ separation.

The $\chi^2$'s for the fits, 210 with 120 degrees of freedom for the momentum-dependent $K$-matrix solution and 197 with 128 degrees of freedom for the constant $K$-matrix solution, are not statistically probable. It should be pointed out, however, that the $\chi^2$ value depends partly on our estimates for the systematic errors and that our data seem to be relatively well fitted.

We may speculate briefly upon the necessity of introducing effective ranges. The addition of the $k^4$ terms into the effective-range parametrization does not change the final amplitudes significantly, and the effective-range amplitudes do not vary more widely than the constant $K$-matrix amplitudes over our momentum region. Furthermore, although the quality of the final two fits is not too different, the constant $K$ matrix does give the lower $\chi^2$, indicating that in this momentum range of 350 to 430 MeV/$c$ the constant $K$ matrix is as good an approximation as the inclusion of effective ranges. The general qualitative agreement of our $S$ waves with those of Martin and Sakitt suggests that it might be interesting to search for a constant $K$-matrix solution covering the whole region from threshold to around 400–450 MeV/$c$.

## V. ISOSPIN MIXING

The principle of charge independence has been tested precisely for several cases involving hadrons with strangeness zero,[23] but few involving strange particles. One violation of charge independence might be that for two particles with similar masses and the same quantum numbers, except for isospin, the physical states would display admixtures of both isospin states. Such mixing has been suggested for the $\Lambda$ and $\Sigma^0$ particles, as well as for the $\eta$ and $\pi^0$ particles which occupy $SU_3$ octet positions analogous to those of the $\Lambda$ and $\Sigma^0$. For the $\Lambda$-$\Sigma^0$ case, for example, the physical states can be described in terms of the pure states and a mixing angle $\theta$ [24]:

$$\Lambda_{\text{physical}} = \cos\theta\,\Lambda_{\text{pure}} + \sin\theta\,\Sigma^0_{\text{pure}},$$
$$\Sigma^0_{\text{physical}} = -\sin\theta\,\Lambda_{\text{pure}} + \cos\theta\,\Sigma^0_{\text{pure}}.$$

The experiments based on $K^-$ absorption in deuterium[25] and associated production by pions in deuterium[26] are the best test of charge independence for the strange particles, but they do not test $\Lambda$-$\Sigma^0$ mixing since the $\Lambda$ and $\Sigma^0$ channels are added to avoid experimental biases.[27]

Since any mixing is expected to be small, we have searched first for an approximate solution assuming isospin purity, as described in Sec. IV. We then include a small complex fraction ($\alpha$) of the $D_{3/2}$ resonant amplitude in the $\Lambda\pi$ amplitudes. Further searching was done, first allowing only $\alpha$ to vary and then allowing all parameters to vary. The two methods give similar results; from the first method we quote $\alpha = (0.02-0.03i) \pm (0.06+0.06i)$. Different solutions with very nearly the same $\chi^2$ and fitted curves give slightly different values of $\alpha$. An average is quoted here and the errors have been increased to reflect the observed differences. 1-standard-deviation contours for our final solution and for an average from different solutions are shown in Fig. 15.

[23] J. J. Sakurai, *Invariance Principles and Elementary Particles* (Princeton U. P., Princeton, N. J., 1964).

[24] R. H. Dalitz and F. von Hippel, Phys. Letters **10**, 153 (1964).

[25] L. W. Alvarez, in *Proceedings of the Ninth International Annual Conference on High Energy Physics, Kiev, 1959* (Academy of Sciences, Moscow, 1960).

[26] J. Button-Shafer, F. S. Crawford, R. Hubbard, M. L. Stevenson, M. Block, A. Engler, R. Gessaroli, A. Kovacs, C. Meltzer, D. Onley, R. Kraemer, M. Nussbaum, A. Pevsner, and P. Schlein, in *Proceedings of the 1962 International Conference on High Energy Physics at CERN* (CERN, Geneva, 1962), p. 272.

[27] However, a rough estimate has been made by R. Chand, Nuovo Cimento **37**, 1789 (1965).

We do not observe any evidence for charge-independence violation on a level of precision which compares favorably with most other relevant experiments. Previous experiments have presented comparisons in terms of cross sections, angular distributions, and polarizations, rather than in terms of amplitudes. These experiments thus set limits only on the square of the isospin-violating amplitude or for small violating amplitudes which interfere maximally with the isospin-conserving amplitude. In our experiment the partial-wave analysis allows us to extract a direct limit on the magnitude and phase of the mixing parameter $\alpha$, and the rapidly varying phase of the $\frac{3}{2}$ amplitude gives rise to comparable sensitivity for any phase of $\alpha$. Thus, we can state an upper limit on the magnitude of $\alpha$:$\alpha$ $\alpha<0.10$ (1 standard deviation). Because the decays

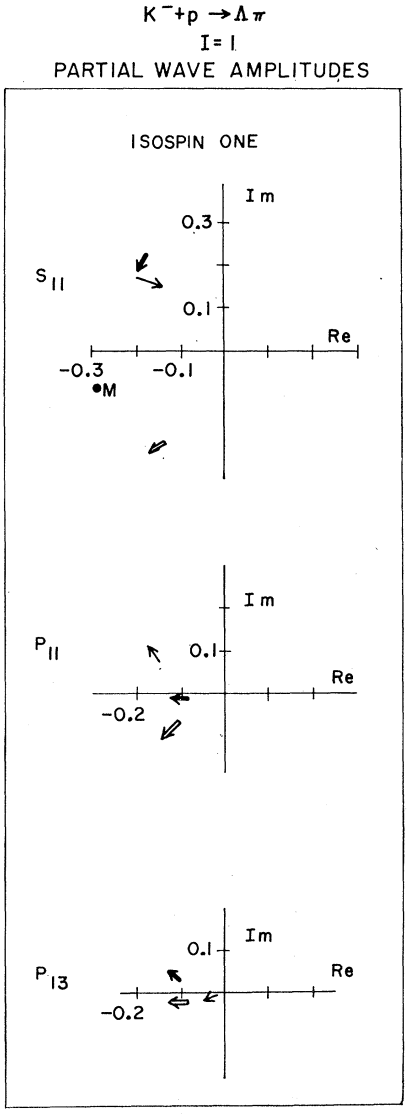


FIG. 14. $K^-+p \to \Lambda\pi$ isospin amplitudes. The meaning of the symbols is the same as in Fig. 12.

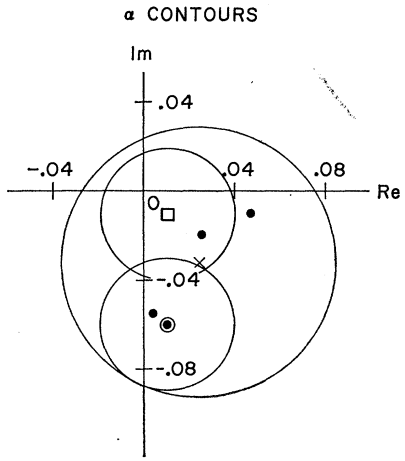


FIG. 15. Contours for the mixing parameter $\alpha$, defined by $T(\Lambda\pi)=T(\Lambda\pi$ background$)+\alpha D_{03}{}^{2\pi}$. The solid points correspond to three different effective-range solutions using only the first term in the effective-range expansion of the $K$-matrix inverse. The circled solid point is the effective-range fit reported in this paper, and the box is the constant $K$-matrix fit of this paper. 1-standard-deviation limits (circular curves) are shown for the two reported solutions. The largest circle encompasses the 1-standard deviation curves of all solutions; its center, the cross at $(0.02-0.03i)$ is the mixing parameter $\alpha$ reported in this paper and in Ref. 1.

$\Lambda(1520) \to \Lambda\gamma$, $\Sigma\gamma$ lead to effects of the order of the statistical errors, increased statistics will not allow the limit from this method to be improved appreciably.

The electromagnetic interaction might be expected to cause a mixing of $\Lambda$ and $\Sigma^0$, and $\eta$ and $\pi^0$. Indeed, Dalitz and von Hippel[24] have related the mixing of these states to the known electromagnetic mass differences, using $U$-spin invariance, with a result which predicts mixing angles $\theta_\Lambda$ and $\theta_{\eta\pi}$ of the order of the errors in our experiment.[28] However, in the $SU_3$ limit, because of the $SU_3$ singlet classification of the $\Lambda(1520)$,[29] the hyperon mixing is nearly canceled by the meson mixing, yielding the prediction $\alpha=\theta_{\Lambda\Sigma}+\theta_{\eta\pi}=-0.013$ $+0.011=-0.002\pm0.002$. Thus our experiment provides merely a consistency check of this theory.

Another possible source of $\Lambda\pi$-$\Sigma\pi$ mixing is isospin impurity of the $\Lambda(1520)$, perhaps due to mixing with the $\Sigma(1660)$. This effect is expected to be small both because the $\Lambda\pi$ branching ratio of the $\Sigma(1660)$ is small and because the 1660-1520 mass difference is larger than the $\Sigma$-$\Lambda$ mass difference.

*Note added in proof.* Preliminary high-statistics LRL data on charged channels near 400 MeV/$c$, reported by R. Tripp at the Duke Hyperon Conference, 1970 (unpublished), indicate a larger elasticity and smaller width for the $\Lambda(1520)$ than the previous (1963) results[7]

[28] A mixing which is slightly larger than that found by Dalitz and von Hippel has been suggested by S. Matsuda, S. Oneda, and P. Desai [Phys. Rev. **178**, 2129 (1969)] on the basis of $SU_2$ and certain assumptions about the nature of $SU_3$ breaking. This mixing is still of the order of the experimental errors, however.

[29] R. D. Tripp, R. O. Bangerter, A. Barbaro-Galtieri, and T. S. Mast, Phys. Rev. Letters **21**, 1721 (1968).

which were available for this analysis. A larger elasticity and smaller width would also agree with recent production experiments as reported by Levi-Setti.[22]


## ACKNOWLEDGMENTS

We wish to express our appreciation for the essential support of the bubble-chamber crew, the Alternating Gradient Synchrotron staff, and the beam-separator group, for the painstaking efforts of the Yale, Massachusetts, and Brookhaven scanning and measuring personnel, and for the free use of the facilities of the University of Massachusetts Research Computer Center. Also, M. Schiff took part in the initial planning of the experiment and was responsible for a large part of the library programming. One of us (J. T.) would like to acknowledge discussions with L. J. Clavelli, N. S. Wong, and M. Sakitt.


## APPENDIX: $\Sigma^0 \to \Lambda+\gamma$ PROPERTIES OF $\Lambda$'s

We now compute the angular distribution in the laboratory center-of-mass system (l.c.m.) [30]

$$\left(\frac{d\sigma}{d\Omega}\right)_{\Lambda \text{ in l.c.m.}} d\Omega_{\Lambda \text{ in l.c.m.}} = \left(\frac{d\sigma}{d\Omega}\right)_{\Sigma \text{ in l.c.m.}} d\Omega_{\Sigma \text{ in l.c.m.}}.$$

Expanding in Legendre polynomials, we have

$$(d\sigma)_\Lambda = a_{l'}{}^\Lambda P_{l'}(\hat{\Lambda}\cdot\hat{K})d\Omega_\Lambda = a_{l'}{}^\Sigma P_{l'}(\hat{\Sigma}\cdot\hat{K})d\Omega_\Sigma$$

(summation notation),

$$\int d\Omega^* \int d\Omega_\Lambda \left(\frac{d\sigma}{d\Omega}\right)_\Lambda P_l(\Lambda\cdot K)$$

$$= \int d\Omega^* \int d\Omega_\Sigma \left(\frac{d\sigma}{d\Omega}\right)_\Sigma P_l(\hat{\Lambda}\cdot\hat{K}),$$

$$4\pi\frac{2}{2l+1}\delta_{l,l'}a_l{}^\Lambda$$

$$= \int d\Omega^* \int d\Omega_\Sigma \, a_{l'}{}^\Sigma P_{l'}(\hat{\Sigma}\cdot\hat{K})P_l(\hat{\Lambda}\cdot\hat{K}), \quad \text{(A1)}$$

where $P_l(\hat{\Sigma}\cdot\hat{K})P_l(\hat{\Lambda}\cdot\hat{K})$ are evaluated in l.c.m. and $d\Omega^*$ is the solid-angle element of $\Lambda$ in $\Sigma$ c.m. system. Choose axes $\hat{Z}=\hat{K}$ and $\hat{y}=\hat{K}\times\hat{\Sigma}/|\hat{K}\times\hat{\Sigma}|$ $(\Phi_{\Sigma,K}=0)$.

[30] The results for the case $\pi^0 \to \gamma+\gamma(\beta'=1)$ are presented in H. L. Anderson, E. Fermi, R. Martin, and D. E. Nagle, Phys. Rev. **91**, 155 (1963). Other discussions of the $\Sigma^0 \to \Lambda+\gamma$ case, particularly the observed $\Lambda$ polarization, may be found in G. Feldman and T. Fulton, Nucl. Phys. **8**, 106 (1958); R. Gatto, Phys. Rev. **109**, 610 (1958); M. H. Cha and J. Sucher, *ibid.* **140**, B668 (1965).

Then

$$(\hat{\Lambda}\cdot\hat{K})_{\text{l.c.m.}} = \cos\theta_{\Lambda,\Sigma}\cos\theta_{\Sigma,K} - \sin\theta_{\Lambda,\Sigma}\sin\theta_{\Sigma,K}\cos\Phi_{\Lambda,\Sigma},$$

$$P_l(\hat{\Lambda}\cdot\hat{K})_{\text{l.c.m.}} = P_l(\hat{\Lambda}\cdot\hat{\Sigma})P_l(\hat{\Sigma}\cdot\hat{K}) + 2\sum_{m=1}^{l}\frac{(l-m)!}{(l+m)!}P_l{}^m(\hat{\Lambda}\cdot\hat{\Sigma})P_l{}^m(\hat{\Sigma}\cdot\hat{K})\cos(m\Phi_{\Lambda,\Sigma})$$

(addition theorem). (A2)

To evaluate $\cos\theta_{\Lambda,\Sigma}$, take axes $\hat{Z}'=\hat{\Sigma}$, $\hat{y}'=\hat{y}$, and $\hat{x}'=\hat{y}'\times\hat{z}'/|\hat{y}'\times\hat{z}'|$ $(\Phi'=\Phi)$. Define

$P=\Lambda$ momentum in $\Sigma^0$ c.m. system,
$E=\Lambda$ energy in $\Sigma^0$ c.m. system,
$\beta=$ (velocity of $\Sigma$ in l.c.m.)$/c$,
$\gamma=1/(1-\beta^2)^{1/2}$,
$\beta'=$ (velocity of $\Lambda$ in $\Sigma$ c.m. system)$/c$,
$\gamma'=1/(1-\beta'^2)^{1/2}$.

Then

$$P_{z'}=\gamma(P\cos\theta^*+\beta E)=\gamma P(\cos\theta^*+\beta/\beta'),$$

$$P_{x'}=P\sin\theta^*\cos\Phi^*=P_{x(\Sigma^0\text{c.m.})},$$

$$P_{y'}=P\sin\theta^*\sin\Phi^*=P_{y(\Sigma^0\text{c.m.})},$$

$$\to \cos\Phi_{\Lambda,K}=\cos\Phi'_{\Lambda,\Sigma}=\cos\Phi^*, \quad \text{(A3a)}$$

$$\Lambda\cdot\Sigma=\cos\theta_\Lambda{}'=\frac{\gamma(\cos\theta^*+\beta/\beta')}{[\gamma^2(\cos\theta^*+\beta/\beta')^2+\sin^2\theta^*]^{1/2}}. \quad \text{(A3b)}$$

Substituting (A2) and (A3a) into (1), one obtains

$$\frac{2}{2l+1}\delta_{l,l'}a_l{}^\Lambda = \tfrac{1}{2}\int d\theta^* \int d\Omega_{\Sigma \text{ in l.c.m.}}\left(\frac{d\sigma}{d\Omega}\right)_{\Sigma \text{ in l.c.m.}} \times P_l(\hat{\Lambda}\cdot\hat{\Sigma})P_l(\hat{\Sigma}\cdot\hat{K})$$

$$= \tfrac{1}{2}\int d\theta^* \frac{2}{2l+1}\delta_{l,l'}a_l{}^\Sigma P_l(\hat{\Lambda}\cdot\hat{\Sigma}),$$

$$\frac{a_l{}^\Lambda}{a_l{}^\Sigma} = \tfrac{1}{2}\int d\theta^* P_l(\hat{\Lambda}\cdot\hat{\Sigma}),$$

$$\frac{a_l{}^\Lambda}{a_l{}^\Sigma} = \tfrac{1}{2}\int d\theta^* P_l \times\left(\frac{\gamma(\cos\theta^*+\beta/\beta')}{[\gamma^2(\cos\theta^*+\beta/\beta')^2+\sin^2\theta^*]^{1/2}}\right); \quad \text{(A4a)}$$

or, changing variables, $\cosh x=\gamma\gamma'(1+\beta\beta'\cos\theta^*)$:

$$\frac{a_l{}^\Lambda}{a_l{}^\Sigma}=\int\frac{\sinh x\,dx}{\gamma\gamma'\beta\beta'}P_l\left(\frac{\cosh x-\gamma'/\gamma}{\beta\sinh x}\right). \quad \text{(A4b)}$$

The coefficients are evaluated for $l=0$–4.

$P_0=1$:

$$\frac{a_0{}^\Lambda}{a_0{}^\Sigma}=\tfrac{1}{2}\int_{\theta_1}^{\theta_2}\cos\theta\,d\theta=\tfrac{1}{2}$$

for the cut actually used, $-1<\theta^*<0$.

$P_1=\cos\theta^*$:

$$\frac{a_1{}^\Lambda}{a_1{}^\Sigma}=\frac{1}{\beta^2\beta'\gamma\gamma'}\left[\sinh x-\frac{\gamma'}{\gamma}x\right]_{x_1}^{x_2}.$$

$P_2=\frac{1}{2}(3\cos^2\theta^*-1)$:

$$\frac{a_2{}^\Lambda}{a_2{}^\Sigma}=\left|_{\theta_1}^{\theta_2}\cos\theta+\frac{1}{2\beta^3\beta'\gamma\gamma'}\left[\frac{3\cosh x}{\gamma^2}+3\left(\frac{\gamma'^2+\gamma^2}{\gamma^2}\right)\ln\tanh\tfrac{1}{2}x-\frac{6\gamma'}{\gamma}\ln(\sinh x)\right]_{x_1}^{x_2}.\right.$$

$P_3=\frac{1}{2}(5\cos^3\theta^*-3\cos\theta^*)$:

$$\frac{a_3{}^\Lambda}{a_3{}^\Sigma}=\frac{1}{2\beta^2\beta'\gamma\gamma'}\left[\left(\frac{5}{\beta^2}-3\right)\sinh x+\left(\frac{-15\gamma'}{\gamma\beta^2}+\frac{3\gamma'}{\gamma}\right)x-\frac{1}{\sinh x}\left(\frac{5}{\beta^2}\right)\left(1+3\frac{\gamma'^2}{\gamma^2}\right)+\frac{5}{\beta^2}\left(-3\frac{\gamma'}{\gamma}-\frac{\gamma'^3}{\gamma^3}\right)\left(-\frac{\cosh x}{\sinh x}\right)\right]_{x_1}^{x_2}.$$

$P_4=\frac{1}{8}(35\cos^4\theta^*-30\cos^2\theta^*+3)$:

$$\frac{a_4{}^\Lambda}{a_4{}^\Sigma}=\frac{1}{8\beta\beta'\gamma\gamma'}\left\{\frac{-17.5}{\beta^4}\left(1+\frac{6\gamma'^2}{\gamma^2}+\frac{\gamma'^4}{\gamma^4}\right)\frac{\cosh x}{\sinh^2 x}+\ln\tanh\tfrac{1}{2}x\times\left[\frac{-17.5\gamma'^2}{\beta^4\gamma^2}\left(-3-\frac{6\gamma'^2}{\gamma^2}+\frac{\gamma'^4}{\gamma^4}\right)-\frac{30}{\beta^2}\left(1+\frac{\gamma'^2}{\gamma^2}\right)\right]+\cosh x\left(\frac{35}{\beta^4}-\frac{30}{\beta^2}+3\right)+\ln(\sinh x)\frac{\gamma'}{\gamma\beta^2}\left(\frac{-140}{\beta^2}+60\right)+\frac{1}{\sinh^2 x}\frac{70\gamma'}{\beta^4\gamma}\left(1+\frac{\gamma'^2}{\gamma^2}\right)\right\}.$$

PHYSICAL REVIEW D VOLUME 1, NUMBER 7 1 APRIL 1970

# Decay Parameters in the Nonleptonic Decay Modes of the Charged Σ Hyperons

D. BERLEY AND S. P. YAMIN
*Brookhaven National Laboratory,* Upton, New York 11973*

AND

S. S. HERTZBACH, R. R. KOFLER, G. W. MEISNER, J. BUTTON-SHAFER, AND S. S. YAMAMOTO
*University of Massachusetts,† Amherst, Massachusetts 01002*

AND

W. HEINTZELMAN,‡ M. SCHIFF,§ J. THOMPSON, AND W. WILLIS
*Yale University,‖ New Haven, Connecticut 06520*

(Received 2 October 1969)

We present the final results of a measurement of the decay parameters for $\Sigma^\pm\to n+\pi^\pm$. We find $\alpha_-=-0.134\pm0.034$ and $\alpha_+=0.037\pm0.049$. Defining $\phi$ by $\beta=(1-\alpha^2)^{1/2}\sin\phi$, $\gamma=(1-\alpha^2)^{1/2}\cos\phi$, we find $\phi_-=(-5\pm23)°$ and $\phi_+=(176\pm24)°$.

## INTRODUCTION

IN this paper, we present the final results[1] of our measurements of the decay parameters in the decays

$$\Sigma^\pm\to n+\pi^\pm. \quad (1)$$

The parameters are defined by

$$\alpha=-2\,\mathrm{Re}(s^*p)/(|s|^2+|p|^2), \quad (2)$$

$$\beta=2\,\mathrm{Im}(s^*p)/(|s|^2+|p|^2), \quad (3)$$

$$\gamma=(|s|^2-|p|^2)/(|s|^2+|p|^2), \quad (4)$$

* Work performed under the auspices of the U. S. Atomic Energy Commission.

† Work supported in part by the U. S. Atomic Energy Commission, under Contract No. AT(30-1)-3651, and in part by a faculty research grant of the University of Massachusetts.

‡ Present address: Physics Department, Carnegie-Mellon University, Pittsburgh, Pa. 15213.

§ Present address: Laboratoire Leprince-Ringuet, École Polytechnique, Paris, France.

‖ Work supported in part by the U. S. Atomic Energy Commission.

[1] Preliminary results were presented in D. Berley *et al.*, Phys. Rev. Letters **17**, 1071 (1966); **19**, 979 (1967). The value of $\phi_-$ given in the second of these papers is inconsistent with the convention used therein, though it is consistent with the convention used in this paper.